Department of Precision and Microsystems Engineering

Exploring Polymer geometries for integrated Photonics Ultrasound Sensors

M.R DROUS

Report no : 2024.034
Coach : T.ERDOGAN
Professor : Dr. P.STEENEKEN
Specialisation : OPT
Type of report : Master Thesis
Date : 24 June 2024

Msc Thesis Report

Exploring Polymer geometries for integrated Photonics Ultrasound Sensors

M56035: Msc Thesis

M.R DROUS

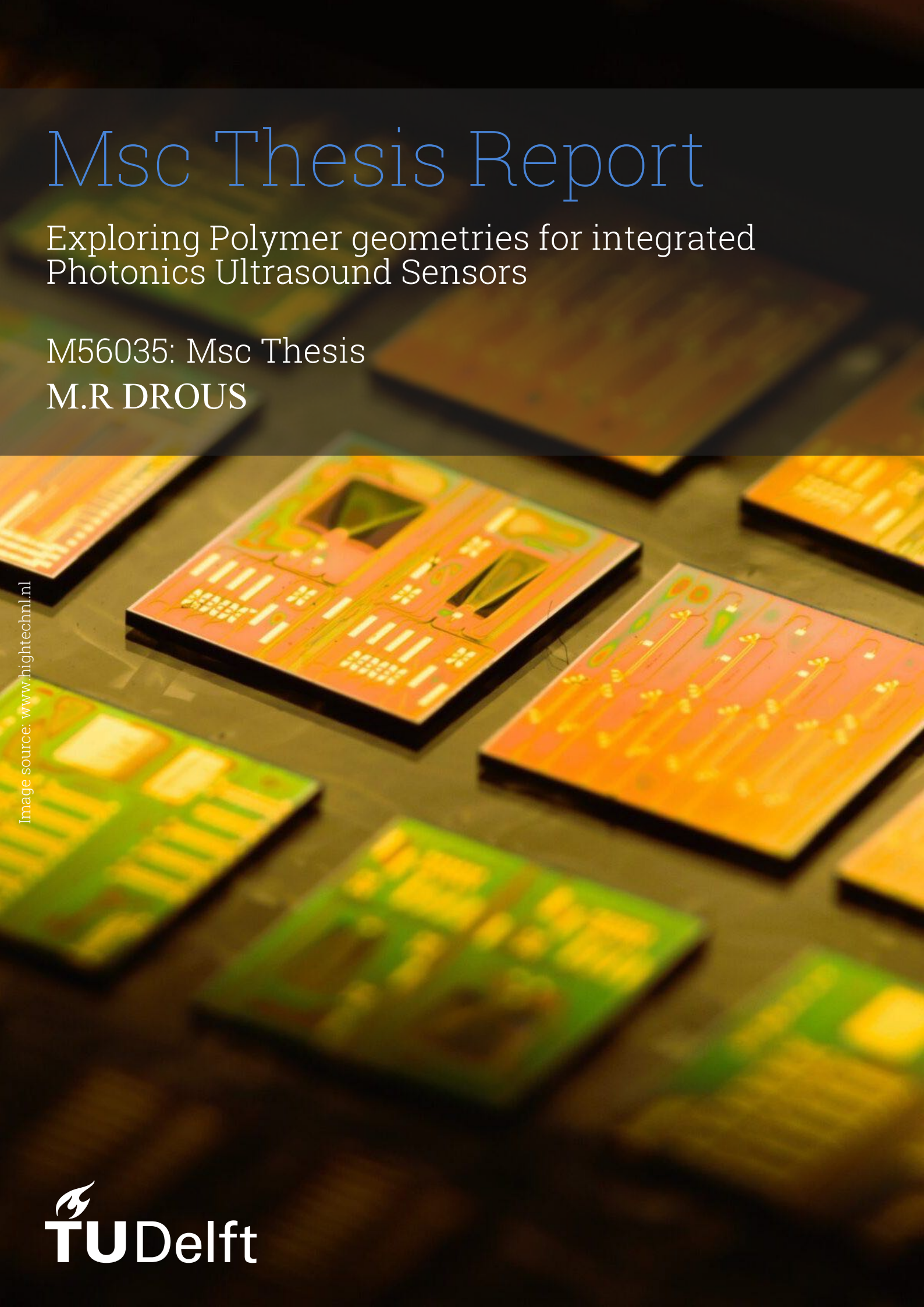

Image source: www.hightechnl.nl

TU Delft

Msc Thesis Report

Exploring Polymer geometries for integrated Photonics Ultrasound Sensors

by

M.R DROUS

Student Name	Student Number
M.R DROUS	5853699

Supervisor:	T. ERDOGAN
Senior Supervisor:	P. STEENEKEN
Project Duration:	Sept, 2023 - July, 2024
Faculty:	Mechanical Engineering

TU Delft

Acknowledgement

I would like to thank my daily supervisor Tufan Erdogan for his continuous support throughout the year. He devoted a great amount time discussing the project and helping me with the optical setup. Next, I would like to thank my senior supervisor Peter Steeneken for advising me and showing great enthusiasm for my project. I would also like to thank Gerard Verbiest for helping me with the data analysis of my measurements. Finally, I would to like to thank all WLAB members for sharing their knowledge and progress during meetings and especially Paulina who dedicated some of her time to print photo-resist patterns with the laser writer.

M.R DROUS
Delft, June 2024

Contents

1

Introduction

In recent years, much interest has been developed towards silicon photonics acoustic detectors (also known as SPADE) and especially in the field of photo-acoustic imaging for biomedical applications. The functioning principle of photo-acoustic imaging is that a pulsed laser light is projected into a tissue where part of the light will be absorbed. This absorption will cause a quick thermal expansion of the tissue which generates an ultrasound wave that can be measured to recreate an image of the tissue. The wave would then travel in water before reaching the ultrasound transducers. This method allows great imaging accuracy because of high optical contrasts and high achievable resolution from the high frequencies of ultrasounds [1] [2]. This imaging method is still at the early stages of development and would require further research and development. The most common sensing devices is a micro-ring resonator (MRR). It is a resonance based device that detects the ultrasound by measuring a shift of resonance wavelength caused by the small mechanical deformation or photo-elastic effects due to the US wave. Its sensitivity to US wave remains limited and thus the topic of this thesis will consist of studying polymer cladding geometries to improve the sensitivity of MRR to ultrasounds. The initiatives taken in this project was to build a FEM simulation to study the impact of deformation and photo-elasticity on a waveguide effective refractive index and to attempt several methods for fabricating a polymer geometry on top of a MRR.

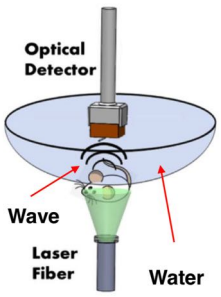

Figure 1.1: Schematic of SPADE imaging for a mouse [2]

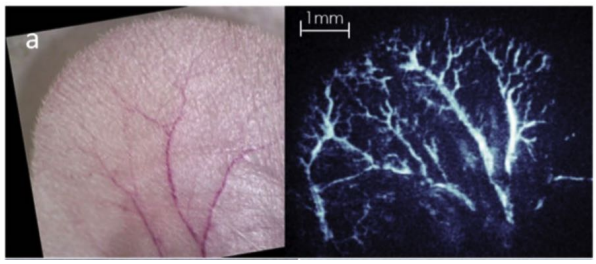

Figure 1.2: Microscope view and SPADE imaging picture [2]

1.1. Background

Optical waveguides are dielectric materials where only light can propagate inside them. In their simplest structural form, light propagates inside a ”core” region which is between an upper and lower cladding. There is an index contrast between the core and the cladding materials such that the core material has a higher refractive index than the claddings. Due to this contrast, light is confined in the core material (figure 1.3). Light can travel using the total internal reflection of the rays and the most common waveguide is the ”strip” waveguide [3].

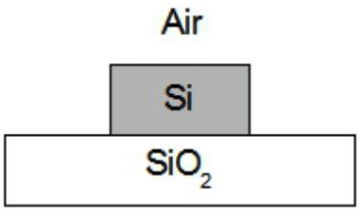

Figure 1.3: Strip Waveguide

There exists 2 methods of modelling light propagation in waveguides. If light is treated as a ray assuming geometrical optics approximations, Snells law can be used to determine the minimum angle θ for total reflection of the ray:

$$sin\theta_c = \frac{n_2}{n_1} \tag{1.1}$$

However, when light rays travel, reflections can cause destructive phase interference's between the waveguide surfaces. To prevent this, the phase of the direction components that are orthogonal to the light propagation direction, must have a phase proportional to 2π and thus only limited amount of possible angles are acceptable.

$$\phi_{total} = 2k_0 n_1 h \cos\theta_1 - \phi_{upper} - \phi_{lower} = 2m\pi \tag{1.2}$$

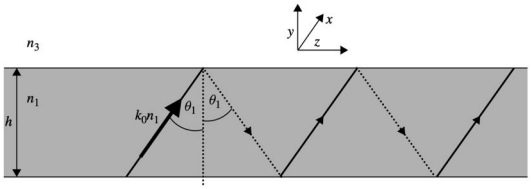

Figure 1.4: Light ray propagation

The ray model approach can be an intuitive approach, but only provides the condition for propagation of light and does not allow using other properties of light such as near field effects (evanescent waves) or even study complex waveguide geometries. The method remains effective only for determining the effective index in planar waveguides (1D) or 2D waveguides with simple geometries and symmetry, thus no further development of this approach will be given. The second method is to treat light as an electromagnetic wave which can provide field equations that allows the study of waveguide geometries by investigating the electric field components.

The book "Silicon Photonics: An Introduction" from Reed and Knights provides very detailed derivations of the propagation of light in 2D planar waveguides, starting from a ray optics approach to a more sophisticated approach that is treating light as an electromagnetic wave [4]. Hence, equations and figures will be used from this book and further details will be added to better understand the relationship between the optical and the electromagnetic aspects.

1.1.1. An electromagnetic model approach

To understand how acoustic waves affect light propagation in waveguides and explain what are electric fields and mode shapes, a derivation of the EM wave is provided. It will show how key properties such as refractive indices and geometries affect electric fields, and how the graphs of these fields are used to evaluate waveguide geometries. It should provide a physical intuition to the reader as well to understand why in later sections, certain materials and geometries can improve WG sensitivity to ultrasounds.

Starting with Maxwell's equations [4]:

$$\begin{aligned} \nabla.\mathbf{D} &= \rho \\ \nabla.\mathbf{B} &= 0 \\ \nabla \times \mathbf{E} &= -\partial\mathbf{B}/\partial t \\ \nabla \times \mathbf{H} &= \mathbf{J} + \frac{\partial \mathbf{D}}{\partial t} \end{aligned} \tag{1.3}$$

The electromagnetic equation is shown below and derivation details can be found in section 2.5 of the book from Reed and Knights [4].

$$\nabla^2\mathbf{E} = \frac{1}{v^2}\frac{\partial^2\mathbf{E}}{\partial t^2} \tag{1.4}$$

As displayed in figure 1.4, light propagates in the z direction and the waveguide cross-sections are in the x and y directions. To solve the wave equation (eq 1.4), it is assumed that there is a TE polarization so the electric field exists only in the x direction written as $\mathbf{E_x}$. When it is polarized only in the x direction, the field is uniform so the double spatial derivative with respect to x will equal to zero but there is also the polarisation in y that still have to be found. For the z direction, the spatial derivative is constant and depends on $\beta = k_z$ since it propagates perpendicularly to the xy plane to infinity.

$$\nabla^2\mathbf{E} = \frac{1}{v^2}(\frac{\partial^2\mathbf{E_x}}{\partial y^2} + \frac{\partial^2\mathbf{E_x}}{\partial z^2}) \tag{1.5}$$

$$\frac{\partial \mathbf{E_x}}{\partial z} = -j\beta\mathbf{E_x} \tag{1.6}$$

So the solution of equation 1.5 is where the complex amplitude $\mathbf{E}_x(y)$ is a function of y that has to be determined.

$$\mathbf{E_x} = \mathbf{E_x}(y)e^{-j\beta z}e^{j\omega t} \tag{1.7}$$

$$\frac{\partial^2\mathbf{E_x}}{\partial y^2} = -\omega^2\mathbf{E_x} \tag{1.8}$$

Thus

$$\frac{\partial^2\mathbf{E_x}}{\partial t^2} = (\beta^2 - \frac{-\omega^2}{v^2})\mathbf{E_x} = (\beta^2 - k_0^2 n_i^2)\mathbf{E_x} = (k_{yi}^2)\mathbf{E_x} \tag{1.9}$$

Where k_{yi}^2 will be the core(c), upper(u) or lower layer(l)

Using again the general equation 1.7, the electric field equation can be solved for each layer:

$$\mathbf{E_x}(y) = \mathbf{E_c}e^{-jk_{yc}y} \textit{ and } \quad \mathbf{E_x}(y) = \mathbf{E_u}e^{-jk_{yu}(y+0.5h)} \textit{ and } \quad \mathbf{E_x}(y) = \mathbf{E_l}e^{-jk_{yl}(y-0.5h)} \tag{1.10}$$

$\mathbf{E_u}$ and $\mathbf{E_l}$ could be rewritten as a function of $\mathbf{E_c}$:

$$\mathbf{E_u}(y) = \frac{k_{yc}}{k_{yu}}\mathbf{E_c}\sin(k_{yc}\frac{y}{2} + \phi) \textit{ rearanged as } \quad \tan^{-1}\left[\frac{k_{yu}}{k_{yc}}\right] = k_{yc}\frac{y}{2} + \phi + m\pi \tag{1.11}$$

After the same is done to the lower layer, the eigenvalue equation 1.12 is obtained by combining the equations in 1.10 and 1.11.

$$\tan^{-1}\left[\frac{k_{yu}}{k_{yc}}\right] + \tan^{-1}\left[\frac{k_{yl}}{k_{yc}}\right] = k_{yc}h + m\pi \tag{1.12}$$

This is similar to the eigenvalue equation obtained from the ray optics approach shown below.

$$[k_0 n_1 b \cos\theta_1 - m\pi] = \tan^{-1}\left[\frac{\sqrt{\sin^2\theta_1 - (n_2/n_1)^2}}{\cos\theta_1}\right] + \tan^{-1}\left[\frac{\sqrt{\sin^2\theta_1 - (n_3/n_1)^2}}{\cos\theta_1}\right] \tag{1.13}$$

However, with the electromagnetic one, it is possible to see what the mode would look like since the field components are included. Furthermore, the electromagnetic equations allows to study different geometries and allows to incorporate stress optic coefficients when solving the equations numerically.

After normalizing the k_{yl}, k_{yc} and k_{yu} vectors in equation 1.12, the equation will be the same as the mode shape equation for the ray approach (see equation 1.13), though the equation itself only describes the condition to be met for light to propagate and does not give any graphical information. Nonetheless, it is equation 1.11 that describes the electric field components in space and in all layers because it allows interface coupling between the core and the claddings. Thus, solving the equation for the spatial electric field components ($\mathbf{E_c}$, $\mathbf{E_l}$ and $\mathbf{E_u}$) will give the electric field value in all locations and plotting them will show what the mode shapes would look like (must be done numerically with a FEM software).

Waveguide designs are evaluated by looking at their mode shapes which describe how the electrical field and power is distributed across the cross section of the waveguide. It is very useful to understand "near field effects" as they allow coupling between different waveguides, show how confined is the optical power so actions can be taken to prevent dispersion, and show how the cladding materials interacts with the core material.

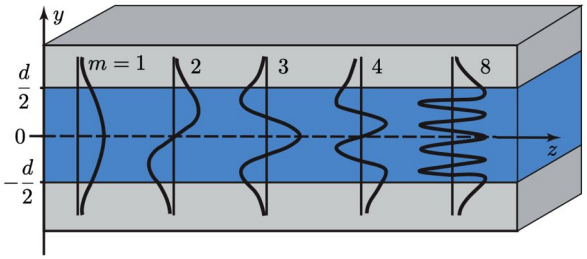

Figure 1.5: Mode profiles of 1D waveguide [5]

1.1.2. Micro-ring resonators

Micro-ring resonators (MRR) are widely used for ultrasound imaging as they are compact in size, provide strong optical fields and have a high quality factor (Qfactor). When they are employed as detectors for photoacoustic imaging, they can have an ultra-broad bandwidth (much broader than piezo) and have a wide angular response which makes them ideal devices for photo-acoustic imaging [6].

A MRR is a device that consists of a bus waveguide with a ring waveguide (WG). There is a very small space gap between them which allows their evanescent fields to interact with each other. When light travels in the bus waveguide, part of the light energy will propagate as well in the ring depending on the wavelength and the ring diameter. At resonance wavelength, destructive interference occurs between the light traveling in the bus WG and the light that travelled inside the ring after doing a 360deg turn. This light in the MRR remains therefore trapped in the ring and at the end of the bus WG a drop of intensity occurs. The frequency spectrum of the transmitted light intensity of the bus WG is "notch-filter" like in figure 1.6. MRR are mainly used for filtering certain frequencies and for detecting changes of refractive indices [7]. When the effective index of the waveguide changes, it affects the resonance condition of the micro ring resonator. The resonance wavelength of the micro ring will then shift because of variations in the effective index that could be caused by changes in the surrounding medium's refractive index (since the effective index depends on the indices of the cross section of the waveguide). By measuring this shift in the resonance wavelength, one can quantify changes in the effective refractive index [7].

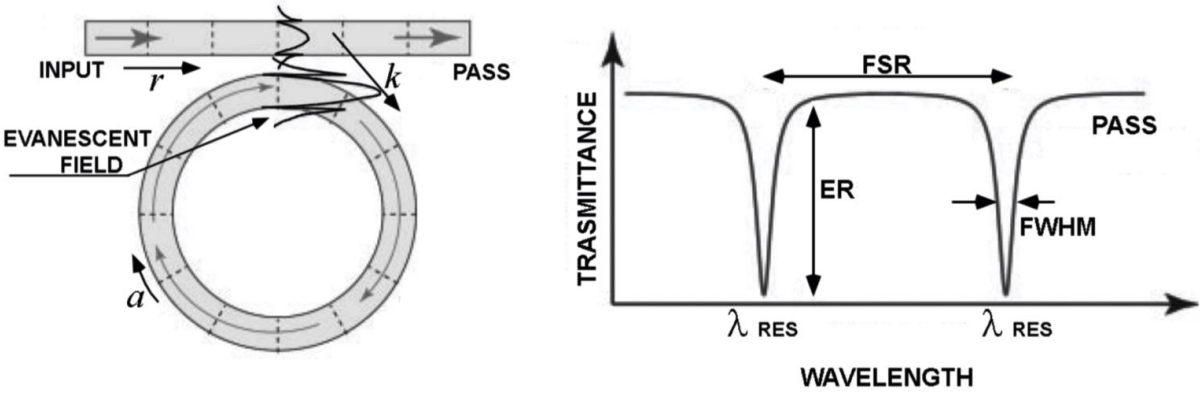

Figure 1.6: Micro-ring resonator schematic and spectrum [8]

The resonance frequency depends on the effective refractive index and the circumference of the circle as shown in equations 1.14, thus any change in the resonance frequency that can be detected in the transmission graph will determine the change of effective index. Hence, making it a compelling detection mechanism for experimental setups. The equations given below will be used to determine and analyse the frequency spectrum and characterise the MMRs in a physical setup. For instance, determining the coupling coefficients based on the resonance peaks shapes, intensity transmission plots or determining the resonance shifts to compute sensitivity values.

$$\lambda_{res} = \frac{n_{eff} L}{m} \quad \Delta_{\lambda_{res}} = \frac{\Delta_{n_{eff}} L}{m} \tag{1.14}$$

Where n_{eff} is effective index, L is ring length, m is the mode number.

In optical experimental setups, the output light intensity is measured by using a photo-detector. The following equation 1.15 corresponds to the transfer function between the input and output intensities of an all pass ring. The term a is the one round trip coupling amplitude transmittance and r is the bus waveguide coupling coefficient, respectively. It is assumed that there is lossless coupling so κ and r have the relationship shown in equation 1.16 [7]. It should be noted that these coupling coefficients are determined experimentally or numerically with simulations.

$$T_{\mathrm{n}} = \frac{I_{\mathrm{pass}}}{I_{\mathrm{input}}} = \frac{a^2 - 2ra\cos\phi + r^2}{1 - 2ar\cos\phi + (ra)^2} \tag{1.15}$$

Equation 1.16 assumes that energy is conserved because no losses occur in the coupling region and that the energy that has escaped the bus waveguide went directly to the cross coupling coefficient κ.

$$|\kappa|^2 + |r|^2 = 1 \tag{1.16}$$

The transmission equation T_{n} (1.15) shows when the intensity in a bus waveguide drops when resonance occurs in the ring. ϕ is the phase such that $\phi = \beta * L$ where β is a propagation constant of the propagating mode. Whenever the phase is a multiple of 2π, resonance occurs in the ring and a drop of intensity occurs in the bus waveguide [7].

The transmission transfer function can be computed in MATLAB for analysis. Concerning the peaks, a high Q-factor is highly desirable because it gives a very narrow resonance peak. With that, when the waveguide will undergo a change of effective refractive index, the shift of the resonance peak will be more pronounced and thus the device will be more sensitive. The width of the peak is defined as the ”full width at half maximum” (FWHM) which is the width of the peak at the points where the curve’s amplitude is half of its maximum value. In addition to that, a high Q-factor lowers the power

consumption, and lowers the filtering at the vicinity of the region of the resonance wavelength [7]. The Qfactor and FWHM equations are useful for comparing ring designs to see how sharp their resonance peak is and what is their coupling efficiency.

$$\text{Qfactor} = \frac{\lambda}{\Delta\lambda} = \frac{\lambda}{\text{FWHM}} \tag{1.17}$$

$$\text{FWHM} = \frac{(1-ra)\lambda_{\text{res}}^2}{\pi n_g L\sqrt{ra}} \tag{1.18}$$

$$n_g = n_{eff} - \lambda_0 \frac{dn_{eff}}{d\lambda} \tag{1.19}$$

where n_g is the group index.

1.1.3. Optical ultrasound detection

Ultrasounds can be detected by measuring the change of the effective refractive (n_{eff}) of a waveguide which is a property dependant on the material refractive index and the geometry of the waveguide. When an ultrasound pressure reaches a waveguide, deformation causes a change of geometry which changes condition of the light travelling, and the n_{eff} value will change. But in addition to that, internal stresses will be contained in different regions of the material due to material elasticity. At the atomic level, displacements in the lattices of the crystalline structure of the material occur, and the refractive index changes [9]. This is known as photo-elasticity (or stress birefringence) and in the following section, the relevant equations will be introduced to describe this phenomenon. The change of refractive index of a material can be related to 2 mechanical properties of materials, namely stress and strain using the photo-elastic tensor [10].

$$\Delta\left(\frac{1}{n^2}\right)_i = p_{ijlm}\varepsilon_j \tag{1.20}$$

Where Δ describes the change (or difference) in n^{-2}, p_{ijlm} is the photo-elastic tensor and ε is the strain.

The photo-elastic tensor is a general tensor for anisotropic media that includes shear stress terms but they can be disregarded because the acoustic wave travels in a fluid where only principle stresses exist (no shear stresses). The pressure wave is approximated to be planar and will be parallel to the top surface of the waveguide so only compression can occur. Only principle stresses (xx,yy,zz) are considered and the photo-elastic tensor can be written as p_{ij} [9].

Finally, the change of refractive index in each direction can be written as:

$$n_i - n_0 = -\frac{1}{2} n_0^3 p_{ij}\varepsilon_j \tag{1.21}$$

Where n_i is the resulting refractive index and n_0 is the initial refractive index.

The stress-optic coefficients (C_1 and C_2) are derived using the principal stresses assumption (σ_x, σ_y and σ_z) and Young's modulus and Poisson's ratio [9]. The stress optic coefficient is a measure of how much the refractive index of a material changes in response to compression. The equations below were derived from Hooke's Law and applied to isotropic materials.

$$\begin{aligned} C_1 &= \frac{n_0^3}{2E}\left(p_{11} - 2vp_{12}\right) \\ C_2 &= \frac{n_0^3}{2E}\left(-vp_{11} + (1-v)p_{12}\right) \end{aligned} \tag{1.22}$$

Where E is the Young's Modulus and v is the poisson's ratio. Finally, using the principle stress only, the following equations can be written.

$$
\begin{aligned}
n_x - n_0 &= -C_1\sigma_x - C_2\left(\sigma_y + \sigma_z\right) \\
n_y - n_0 &= -C_1\sigma_y - C_2\left(\sigma_z + \sigma_x\right) \\
n_z - n_0 &= -C_1\sigma_z - C_2\left(\sigma_x + \sigma_y\right)
\end{aligned} \tag{1.23}
$$

Every material have different stress optic coefficients and polymers are known to be soft materials and can deform easily. Increased deformation gives them, high stress optic coefficients compared to other materials and makes them a material of choice for claddings. In a paper, it was demonstrated that by applying a PDMS coating on a MRR waveguide, the cladding has increased the MRR sensitivity to ultrasounds [11].

1.1.4. Ultrasound induced resonance shift

Changes of effective refractive indices in a MRR can be determined by measuring a shift of resonance wavelength as shown in eq 1.14. The acoustic pressure will cause a slight deformation in the MRR which will change the effective refractive index and the resonance peak will shift [6]. The measurement principle is to use the intensity spectrum of a MRR and set the laser wavelength to the wavelength value that has the highest slope of light intensity derivative with respect to wavelength (see red curve in the figure below). It is at this location where the smallest shift of wavelength can be identified [12]. By observing the transmitted intensity variation over time, the disturbance peak values can be recorded. Using the intensity graph, values of the intensity can be matched to the corresponding wavelengths and the amount of shift can be determined (green and blue curve) [12].

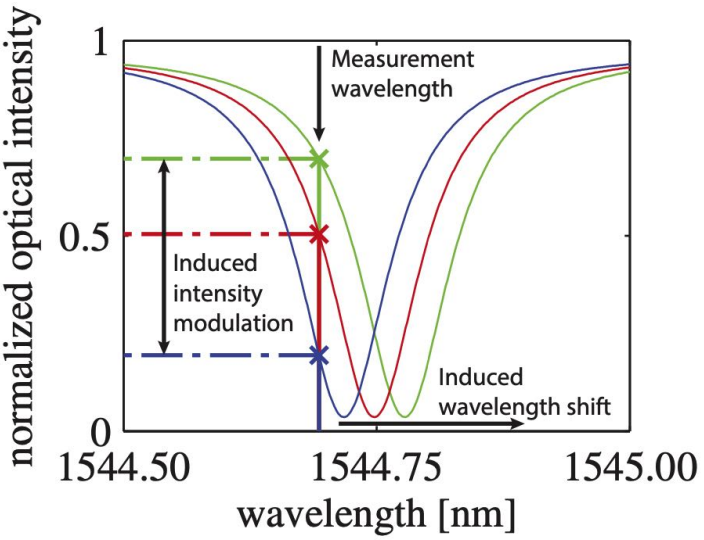

Figure 1.7: Intensity curves of different peak intensity values [13]

1.1.5. Ultrasound sensors

Currently, the most popular types of ultrasound sensors are piezo-transducers which have piezoelectric materials that converts pressure into electrical signals and vice versa. Other types of transducers include piezoelectric micromachined ultrasound transducers (PMUT) and capacitive micromachined ultrasound transducers (CMUT) which uses the capacitive effect of membranes [3]. For photo-acoustical imaging, the sensitivity and bandwidth of ultrasound sensors are crucial properties for producing accurate images. However, significant physical limitations exist in piezo-transducers such as difficulties in miniaturization where the sensors array sizes cannot be made smaller and thus the resolution cannot be increased [6]. They only capture a small part of the acoustic signals due to their limited bandwidths and acceptance angles. Thus, there will be more losses of information causing limited image resolutions. Also they are prone to strong electromagnetic fields, unlike optical-acoustic sensors which are

made of dielectric materials. They are an effective alternative for detecting ultrasounds and have been demonstrated to have higher sensitivities and broader detection bandwidths compared to piezoelectric transducers [6]. Common optical-ultrasound devices are Micro-Ring resonators (MRR), fiber Bragg grating (FBG), Fabry Perot (FP), and Mach-Zehnder interferometers [14]. They have high sensitivities and high capabilities to be miniaturized and are often utilized for biomedical applications. In the literature, micro-rings resonators (MRR) have been widely studied because of their compact size, ultra-broad bandwidth (much broader than piezo), high quality factor (Qfactor) and compatibility with CMOS technology thus only MRR based ultrasound detection is considered in this thesis [6].

1.1.6. State of the art

Few papers have been selected about state of the art MRR sensors and the most important characteristics have been given such as design, materials, fabrication methods and performance.

A PDMS polymer MRR was fabricated by Rong et al. using nanoimprint lithography to make a silicon master mold from which the MRR mold was made. A protective layer was added for better stability inside water. It has a bandwidth of 23MHz, Q factor of 4.6e4, a signal to noise ratio of 83 and acceptance angle of 90deg [15].

Ding et al. have designed an SU8 polymer cladded MRR with a 10um radius, offering a 7.4e4 Q-factor, a signal to noise ratio of 65Pa, NEP of $14.5mPa/\sqrt{Hz}$, bandwidth of 20MHz and a sensitivity of 183.3mV/kPa. The polymer was deposited using electron beam lithography which provides very high resolutions but is not cost effective [16].

Nagli et al. have designed a Bragg grating ultrasound sensor where a bragg grating is fully coated with a layer of BCB, glass and gold at the very top surface. The glass has a concave region that functions like a lens for guiding the ultrasound wave. The sensors has a NEP of $37mPa/\sqrt{Hz}$ and a bandwidth of 84MHz [17]. Despite the fact that it is not a MRR, the ease of manufacturing and very high bandwidth makes it a relevant sensor.

W.Westerveld et al., have designed a MRR with a suspended membrane and very small air gap of 15nm between the MRR and the membrane. It has a NEP of $1.3mPa/\sqrt{Hz}$, a bandwidth of 30MHz and a maximum sensitivity of 2.5mV/Pa which makes it currently the most sensitive sensor. However, the very small gap puts a physical limit on maximum actuation movement and the fabrication method is more complex compared to other MRR designs due to the several steps needed for making the suspended membrane [12].

Name	MRR	Sensitivity	Bandwidth	NEP
W.Westerveld	MRR with suspended membrane	$2.5mV/Pa$, $35fm/Pa$(shift)	$30MHz$	$2.3mPa/\sqrt{Hz}$
Nagli et al.	Bragg grating with BCB coating	Not available	$84MHz$	$37mPa/\sqrt{Hz}$
Ding et al.	SU8 cladded MRR	$0.18mV/Pa$	$20MHz$	$14.5mPa/\sqrt{Hz}$
Rong et al.	PDMS MRR	Not available	$23MHz$	$83Pa$
Zarkos et al.	Electronic/photonic sensor	$40fm/kPa$(shift)	$5MHz$	$935Pa$

Table 1.1: Sensitivity results comparison

1.1.7. Literature review and research gaps

Based on the available literature and current state of the art sensors, 2 research gaps were identified and require further investigation. There has been no attempts to study the upper cladding geometry for improving sensitivity induced by either photo-elasticity or deformation. Depending on the pressure induced internal stresses location, the change of material refractive index will not be the same everywhere. The geometry can be thus be modified to cause higher stresses in targeted regions with high electric fields intensity as these regions are more sensitive to changes of refractive index as explained in reference [12]. Another research gap, is that it is not clear in which situation photo-elasticity or waveguide deformation will be the dominant cause of change of refractive index. Therefore, there might multiple possible designs that improve sensitivity.

1.2. Thesis project

1.2.1. Research objective and proposal

As a continuation to the ongoing research done in the DMN department (WLAB) regarding photonics sensors, a study of polymer cladding geometry will be done to attempt to improve micro rings sensitivity to ultrasounds (US) for acoustical imaging purposes. It follows up on a research that was conducted in which the US sensitivity of a MRR was improved by depositing a layer of PDMS on top. It showed that sensitivity to ultrasounds was reasonably increased and a conference paper was published (see: [11]). Consequently, the remaining aspect of the cladding to be studied is its geometry, where currently no literature is available yet on this topic. In this thesis, it will be attempted to fill this current research gap with the following research question:

Could the sensitivity of MRRs to ultrasounds be improved by using a patterned polymer cladding?

To address this research question, the planning and main procedures are cited below:

- Building a valid acoustic and electromagnetic wave finite element model. This model would be evaluated against numerical computation of an analytical method.
- Conducting a parametric study of cladding height, width and applied pressure for determining deformation and photo-elasticity sensitivity. This would allow to find at which dimensions, deformation or photo-elastic effect would be the dominant effect. Later on, it could serve as a base model for comparing different cladding designs, once the model is verified against results of optical ultrasound measurements.
- Attempting different fabrications methods for making a pattern on a polymer cladding. Ideally, a PDMS pattern would be made with the smallest features such that they have dimensions similar to core dimensions. However, it can be quite challenging and feature size, material choice or positioning accuracy may have to be prioritized based on the fabrication results.
- Conducting ultrasound measurements for no cladding, full cladding and patterned cladding waveguides to observe any improvements in ultrasound sensitivity.

This thesis report is organized in 2 main sections. The first section is a model study, where parametric studies of rectangular claddings will be done to understand and differentiate the effects of cladding photo-elasticity and deformation on US sensitivity. The second part is an experimental part where it will be attempted to fabricate polymer cladding geometries using available equipment at the PME department and doing optical-ultrasound measurements to observe any improvements in sensitivity. At the end, ultrasound measurement will be made with the fabricated polymer claddings and compared to the simulations.

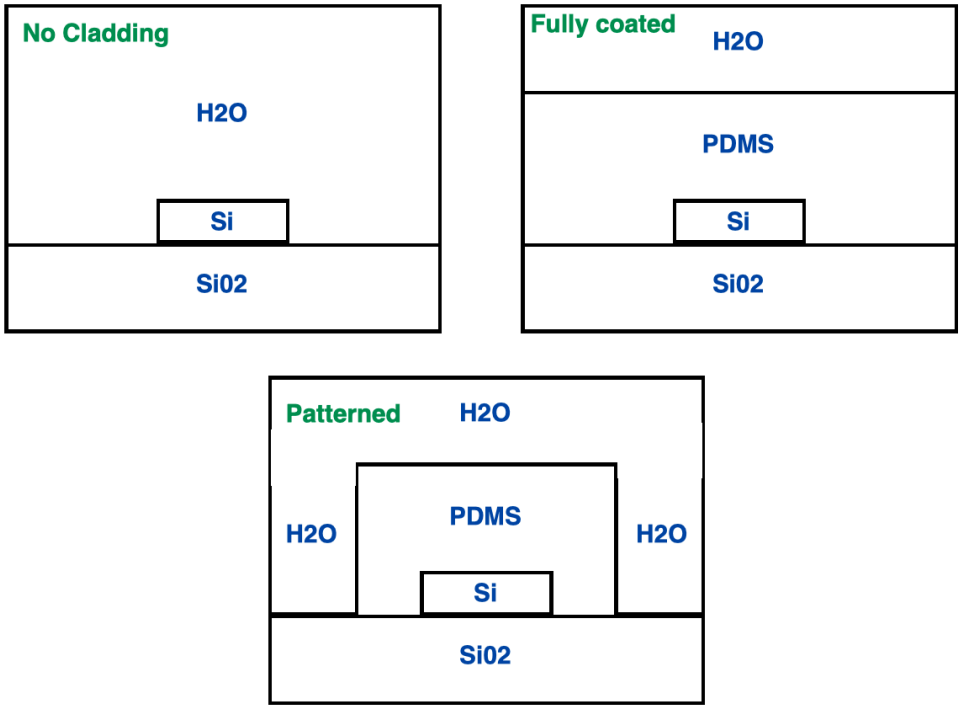

Figure 1.8: Different geometries to be tested

2

Modelling and simulation

In this chapter, includes a section where a COMSOL simulation is setup to first verify and validate a solid mechanics coupled with EM wave physics model. Then a parametric study of cladding height and width is conducted for demonstration and to observe cladding effect on ultrasounds sensitivity. In the last section, the methodology used for simulating different cladding configurations is explained as well as its limitations. The cladding configurations are based on the fabricated polymer geometries which will be compared to the ultrasound measurements in a later chapter.

2.1. Opto-acoustic simulation

In the section below, a simulation of the cross section of a cladded silicon waveguide is conducted.

First, a valid model is built. Then a sensitivity analysis is done by doing a parametric study of cladding dimensions and pressure. This allows to determine effects of the deformation and photo-elasticity on the effective refractive indices where both of these effects are induced by an acoustic wave. The core silicon waveguide has a standard dimension of 0.22μm height and 0.45μm width, so that the simulation and computed effective refractive indices can be compared to available literature. A first acoustic simulation was conducted without computing the electromagnetic wave modes shapes to determine the pressure-like behavior, and determine the appropriate solid mechanics boundary conditions to be applied with the electromagnetic wave simulation.

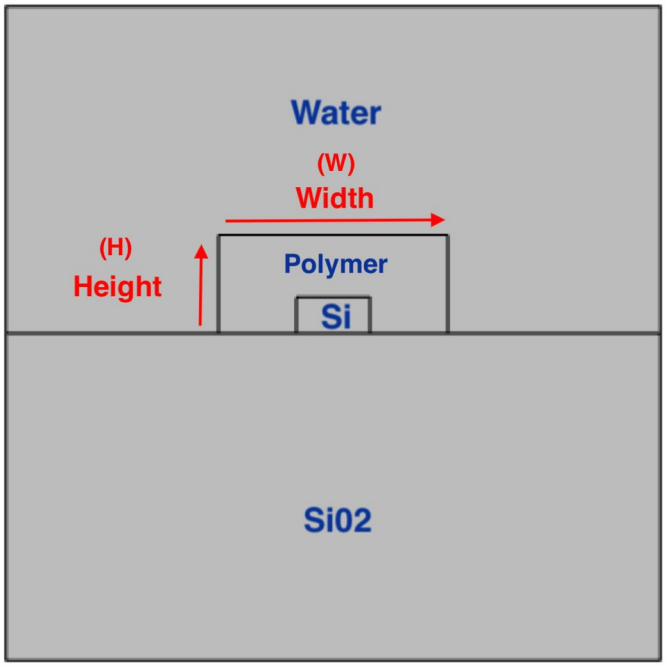

Figure 2.1: Schematic of Waveguide

Note: In the following sections, the cladding width and height will always be referred as the distance between the top, bottom and left and right edges of the polymer region as shown by the red arrows in figure 2.1.

2.1.1. Acoustic simulation

In this acoustics simulation, the dimension of the polymer region were arbitrary chosen to be $1\mu m$ height and $2\mu m$ width because the appropriate dimensions will be determined in the EM wave simulation from doing a parametric study. Figure 2.2 shows the acoustic domain made of water with the blue edges as the coupling interface between the water and the solid waveguide. Perfectly matched layers (PML) are used to remove acoustic reflections from the sides.

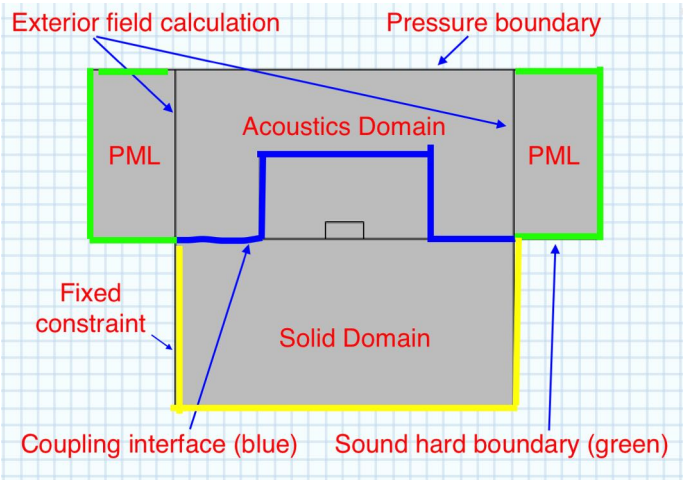

Figure 2.2: Display of solid mechanics and acoustics boundary conditions

Figure 2.3 shows the results of the simulation. The most important aspect to observe is the hydrostatic pressure behavior caused from the top pressure boundary at 31.6MHz and the displacement

graph shows that very well at the boundary between the polymer region and SiO_2 substrate where the deflection was homogeneous.

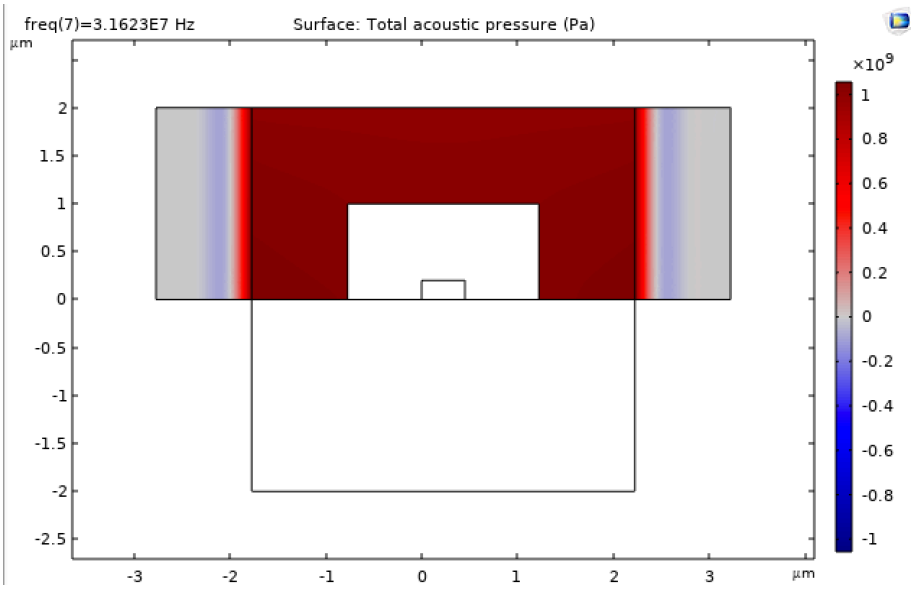

Figure 2.3: Pressure graph

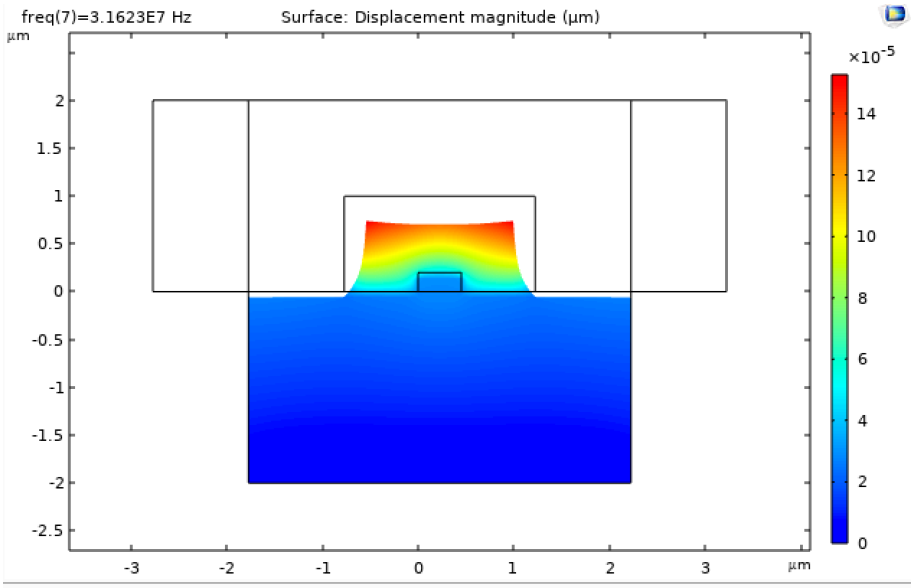

Figure 2.4: Displacement from acoustic domain

A simple calculation can be done to validate the acoustic pressure model. The wavelength equation can be used to compute the wavelength at a frequency of 31.6MHz and sound speed of 1500m/s to determine the scale of the wavelength compared to the maximum height on the water domain.

$$\lambda = \frac{v}{f} = \frac{1500}{3.16e7} = 47.46\mu m \tag{2.1}$$

A common rule of thumb for assuming a hydro-static pressure is that the height (written as H) should be smaller than one sixth of the wavelength for a sufficiently accurate computation.

$$H < \frac{\lambda}{6} \tag{2.2}$$

The maximum height of the water region is 2μm whereas the wavelength is 47.46μm which is around 24 times the height of the water region. Therefore, no standing waves can be observed and the pressure is expected to be the same across the whole water domain. This concludes that the acoustic model is valid and that in the EM wave simulation, a pressure boundary condition can be applied directly to the edges of the polymer region which simplifies the setup of the model by not having to use the acoustic physics module.

2.1.2. EM wave simulation

Finding the effective refractive index can be quite tricky because depending on the setup of the 'Mode analysis' step in the 'Study' section, COMSOL can find effective refractive indices that do not exist in real life and make the results wrong. Therefore a MATLAB program from Dr W.Westerveld (from TU Delft) was used to compute analytically the effective refractive indices and evaluate them against the COMSOL results. The program is available at `https://waveguide.sourceforge.net/`. Since the analytical equation works best with simple geometries (no more than 3 layers), the cladding region (polymer) was removed to first validate the model and then it will be put back. The values are found to be practically the same between the 2 software with a negligible error. Possible causes for deviation from the analytical n_{eff} values, are the mesh sizing and "mode analysis" study set up parameters. The program computes a numerical solution of the wave equation developed by Marcatili which was adapted by Dr W.Westerveld for high contrast waveguides. The following code is an extract from the result of some of the MATLAB results.

For the first mode (named TM-like mode), n_{eff}=1.741 in MATLAB and n_{eff}=1.7458 in COMSOL:

```
*** Effective index using Eigenvalue equations ***
Effective index          [-]           1.741
Effective group index    [-]           4.797
Temperature-shift Neff   [/K]          1.823e-04
```

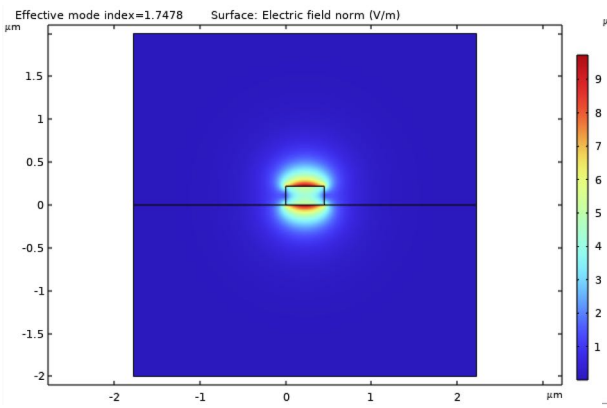

Figure 2.5: Electric field distribution of 1st mode

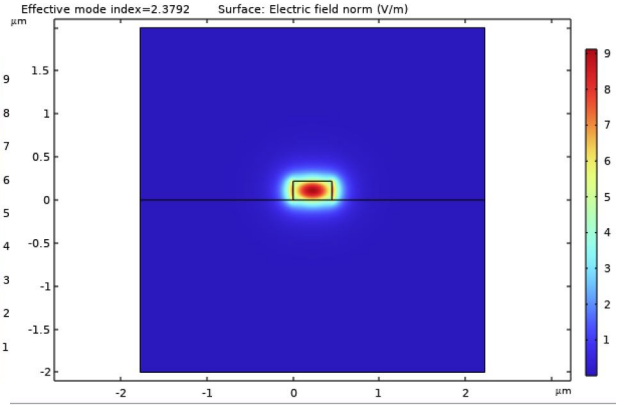

Figure 2.6: Electric field distribution of 2nd mode

For the second mode (named TE-like mode), n_{eff}=2.376 in MATLAB and n_{eff}=2.3792 in COMSOL.

```
*** Effective index using Eigenvalue equations ***
Effective index          [-]           2.376
Effective group index    [-]           4.265
Temperature-shift Neff   [/K]          2.113e-04
```

2.1.3. Preliminary sensitivity analysis

To begin, assuming a 1kPa pressure, will be determined approximately how much change of effective refractive index the pressure will induce. With the assumed pressure, a deformation can be determined from the strain equation which depends on pressure and the elastic modulus. In the following sections, both a patterned and non-patterned cladding COMSOL simulations are used to determine the sensitivity to deformation and photo-elasticity. From there based on the assumed pressure and its induced strain, values of changes of effective refractive index can be calculated.

Deformation and photo-elastic quantities

The strain equation can be used to determine the amount of deformation caused by an applied pressure of 1kPa. For a soft polymer such as PDMS, the young's modulus is around 3MPa. Thus the strain is:

$$\varepsilon = \frac{\Delta L}{L} = \frac{\sigma}{E} = \frac{1 * 10^3}{3 * 10^6} = \frac{1}{3} * 10^{-3} \tag{2.3}$$

Assuming that the core is fully cladded with a rectangular geometry pattern (see figure 1.8, fully coated), with a core height of 0.22μm and cladding height of 1.4μm (effective height is 1.18μm when removing height of core). It is assumed that the core is significantly stiffer than the cladding so only the cladding height deforms. After rounding the effective cladding height to 1.2μm, the deformation is determined to be approximately:

$$\Delta L = \varepsilon * L = \frac{1}{3} * 10^{-3} * 1.2 * 10^{-6} = 0.4 * 10^{-9}[m] \tag{2.4}$$

The effective refractive index (n_{eff}) can be computed with COMSOL, with and without including deformation to see the change of n_{eff}. This will be done in the following sections.

Amount of Photo-elasticity

Ideally, values of the stress-optic coefficients of PDMS would be used since it was demonstrated in literature to be a sensitive polymer and is readily available in the laboratories. However, no values of the stress-optic coefficient were found in the literature. Therefore for this demonstration, the BCB polymer coefficients are used as it is a sensitive polymer and should be of a similar order of magnitude with PDMS.

$$\begin{aligned} n_x - n_0 &= -C_1\sigma_x - C_2\left(\sigma_y + \sigma_z\right) \\ n_y - n_0 &= -C_1\sigma_y - C_2\left(\sigma_z + \sigma_x\right) \\ n_z - n_0 &= -C_1\sigma_z - C_2\left(\sigma_x + \sigma_y\right) \end{aligned} \tag{2.5}$$

Material	Refractive Index	C1 [1/Pa]	C2 [1/Pa]
BCB	1.44	99e-12	31e-12

The equations above are not suitable for a back of the envelope calculation to get an average since these equations are meant for 3D problems. It is when implemented in COMSOL that they can be computed. In a 1D problem, the highest achievable change of n_{eff} can be determined, assuming a 1KPa pressure at one direction, with the highest stress optic coefficient (C_1) will be:

$$\Delta n_{eff} = C_1 * Pressure = 99 * 10^{-12} * 1000 = 99 * 10^{-9} = 10^{-7} \tag{2.6}$$

2.1.4. Sensitivity analysis with FEM

In this section, two models of COMSOL simulations are conducted: Without pattern (fully coated) and with pattern. Parametric sweeps were implemented to evaluate how the n_{eff} changes with respect to the width, height and pressure for both models. The derivatives with the respect to the mentioned parameters were computed and based on an assumed pressure of 1kPa and the deformation of $0.4 * 10^{-9}$ it induces. A graph of change of n_{eff} induced by deformation and photo-elasticity was plotted for

comparison. This section is for demonstration purposes to be able to differentiate the effects that photo-elasticity and deformation have on ultrasound sensitivity. These simulations are made with PDMS claddings.

Full Cladding (without pattern) sensitivity analysis

With a full cladding, only parametric sweeps of the height and pressure are done.

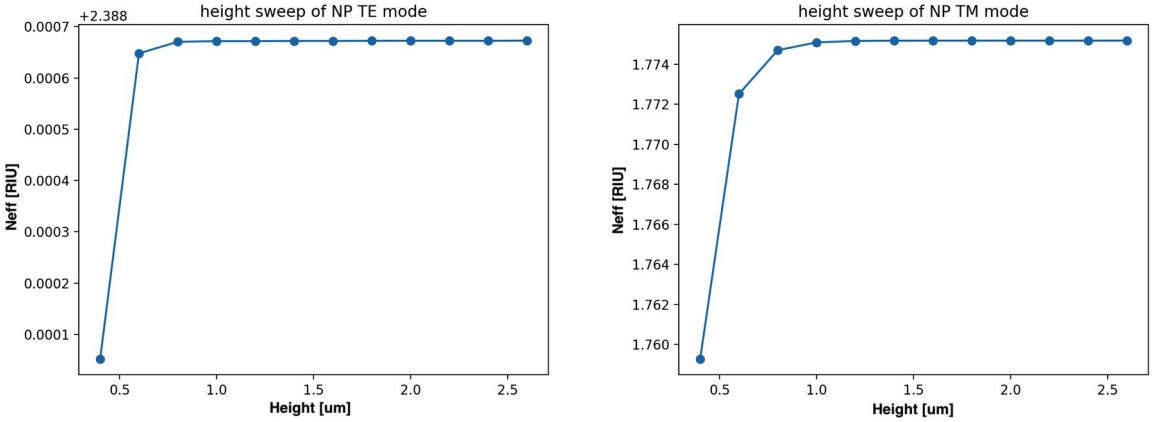

Figure 2.7: Sweep of full cladding (height along x-axis)

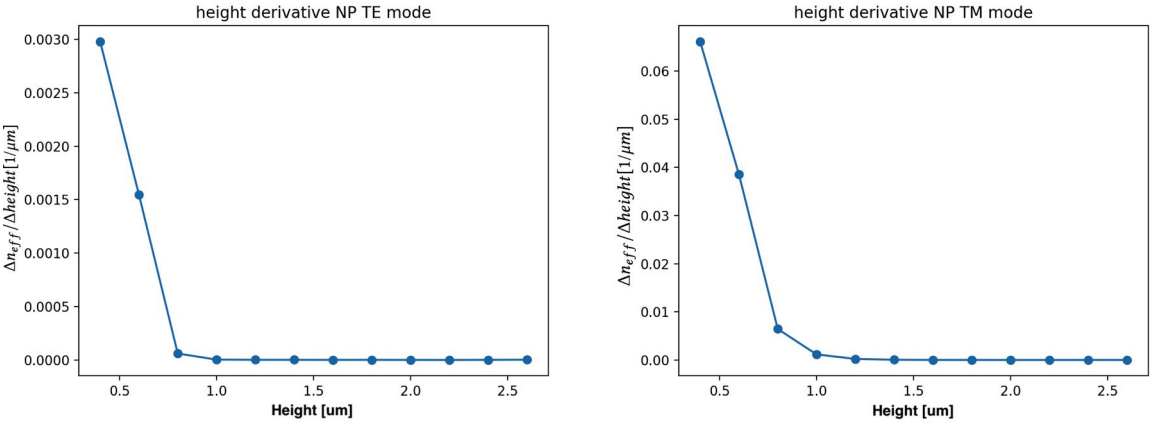

Figure 2.8: $\frac{\Delta n_{eff}}{\Delta height}$ of unpatterned cladding

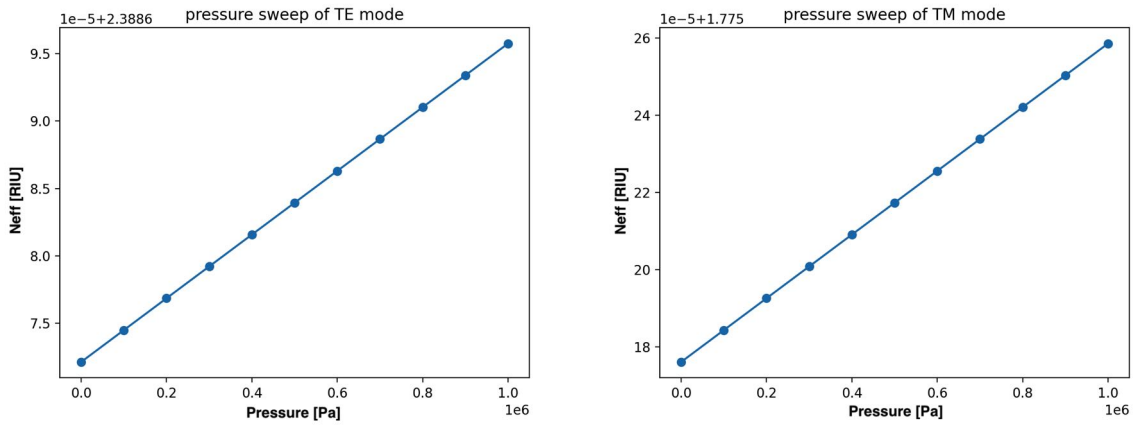

Figure 2.9: Sweep of pressure

The pressure sweep displays a linear behavior and has a derivative of n_{eff} with respect to pressure of $2.36 * 10^{-11}[1/Pa]$ for the TE mode and $8.24 * 10^{-11}[1/Pa]$ for the TM mode

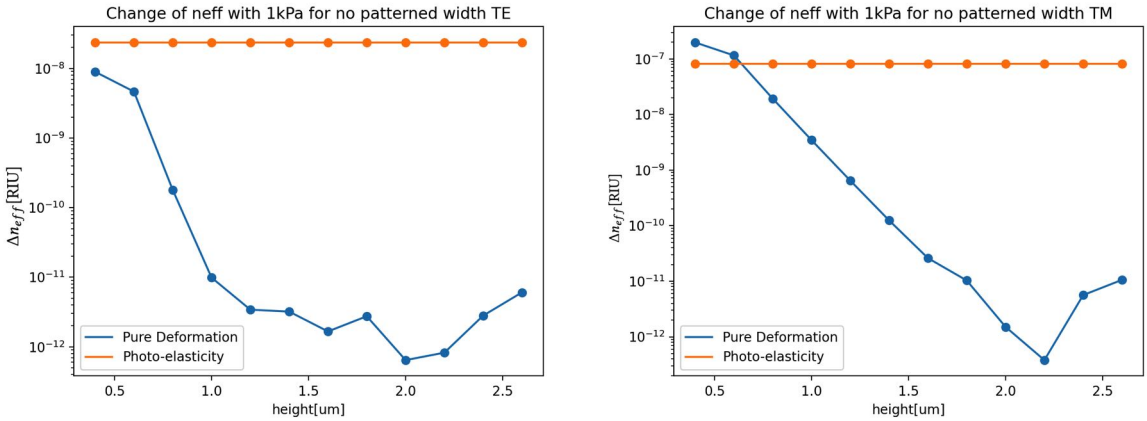

Figure 2.10: Induced change of n_{eff} based on 1kPa pressure and 0.33e-3 strain (eq 2.3) and 1.4μm height (without pattern)

Patterned cladding sensitivity analysis

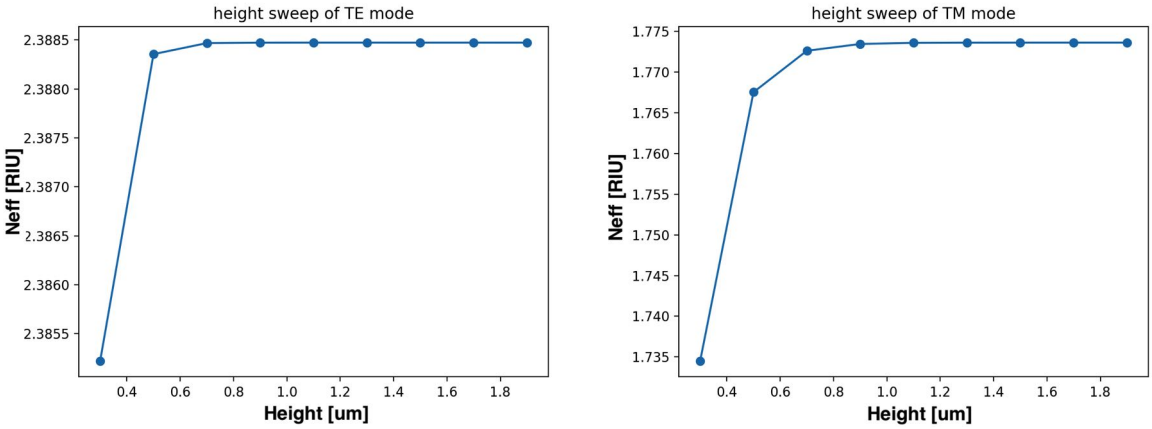

Figure 2.11: Sweep of patterned cladding height

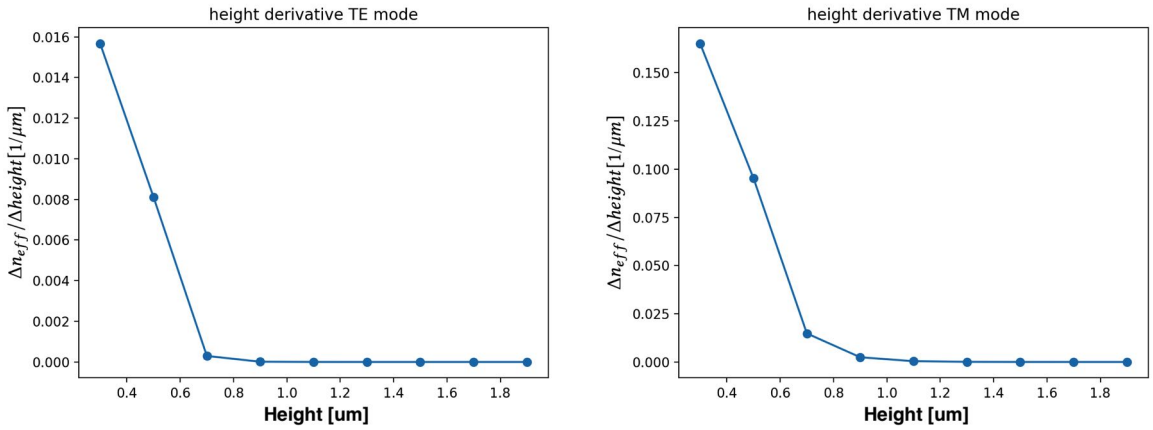

Figure 2.12: $\frac{\Delta n_{eff}}{\Delta height}$ of patterned cladding

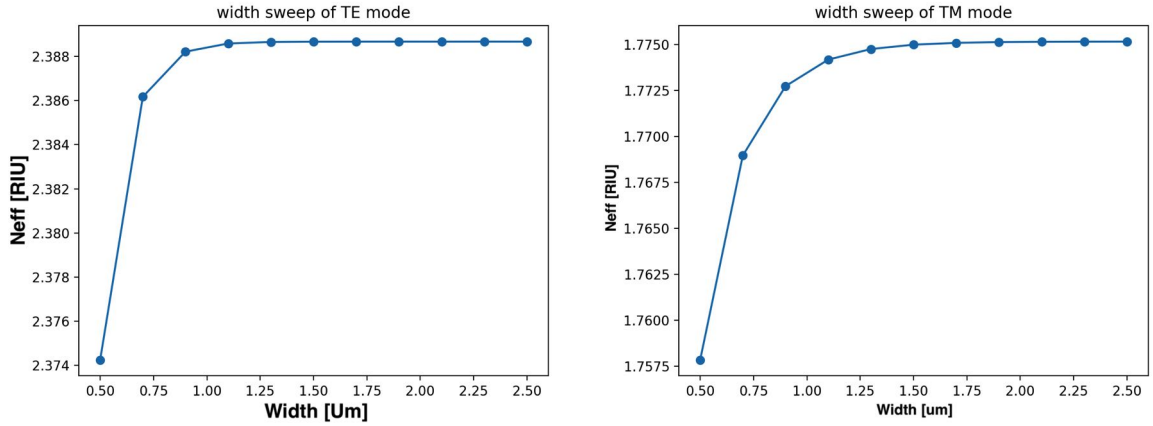

Figure 2.13: Sweep of patterned cladding width

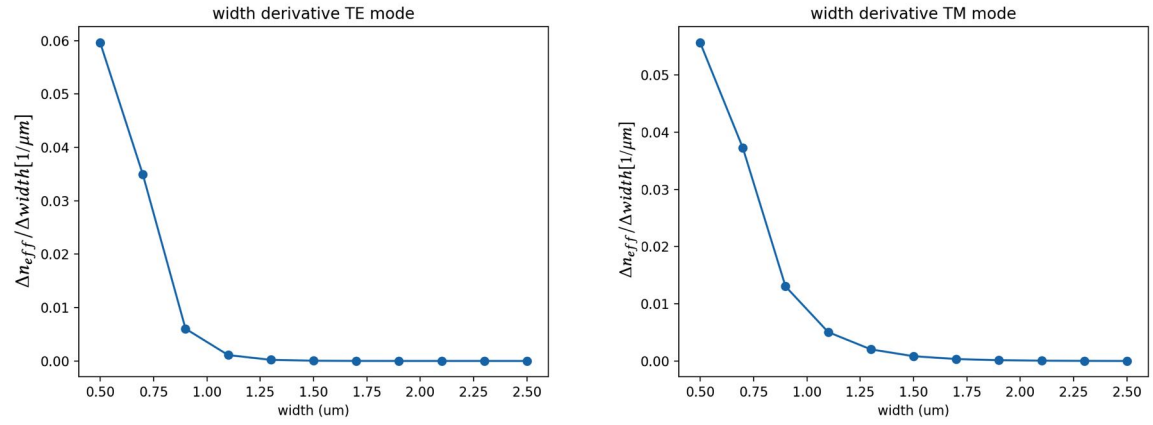

Figure 2.14: $\frac{\Delta n_{eff}}{\Delta width}$ of patterned cladding

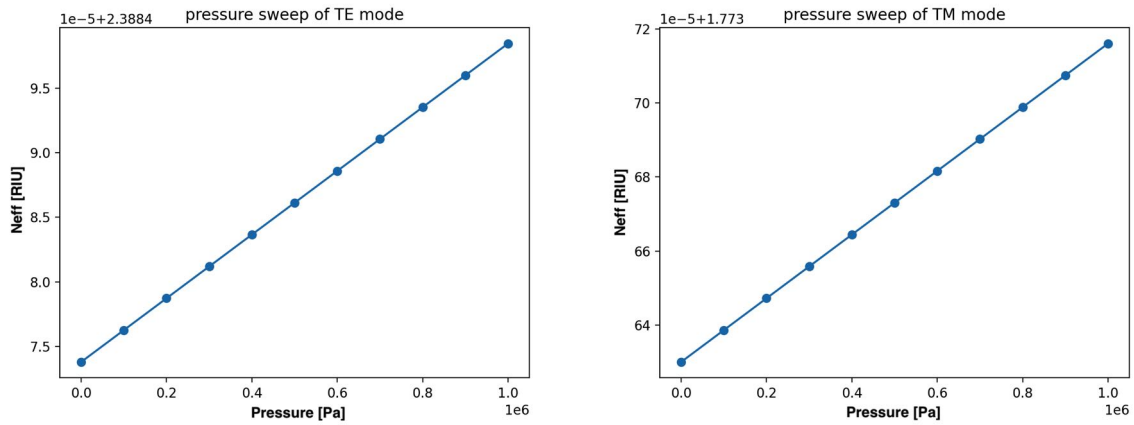

Figure 2.15: Sweep of pressure

The pressure sweep displays a linear behavior and has a derivative of n_{eff} with respect to pressure of $2.46 * 10^{-11}[1/Pa]$ for the TE mode and $8.59 * 10^{-11}[1/Pa]$ for the TM mode.

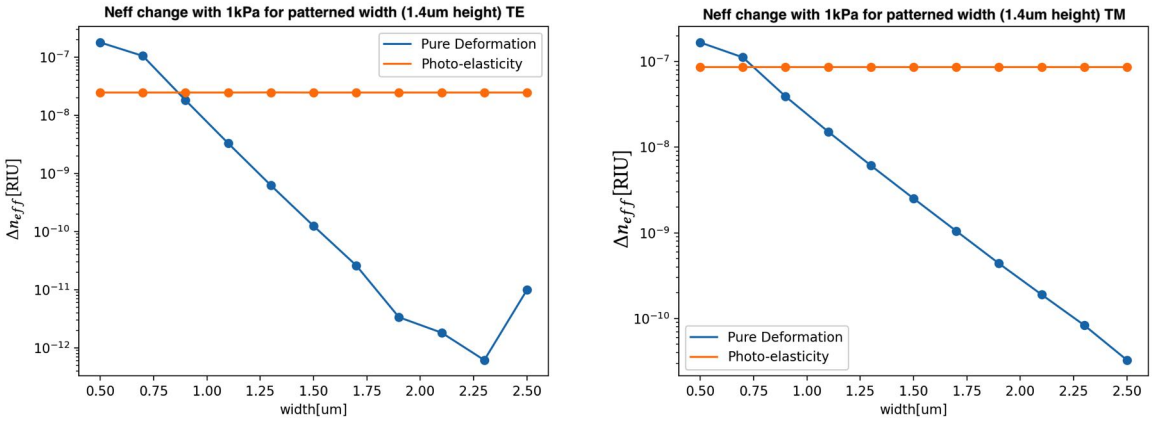

Figure 2.16: Induced change of n_{eff} based on 1kPa pressure and 1/3e-3 strain and 1.4μm height (with pattern)

2.2. Simulation method and its limitations

In this section, the same model as shown in the previous section is used but with different configurations to match the fabricated polymer geometries in chapter 3. It will be explained what materials and geometries were used, what approximations were made and what are the limitations of these models. For all models, a plane strain 2D approximation is used. This assumes that the strain in the Z direction is equal to zero ($\epsilon_z = 0$). The waveguide is assumed to be sufficiently long to withstand deformations in the Z direction, so there will only be internal stresses in that direction. The change of n_{eff} is determined from first computing the simulation with no pressure applied to obtain the initial value of the n_{eff}. Then the new n_{eff} is computed by adding the pressure which creates deformation and photo-elasticity. The deformation effects are included by computing the electric field with the new geometry (using the deformed mesh) and the photo-elastic effects are included by adding manually the equations 1.23 as variables in the geometry domains and using the spatial stress components of the deformed mesh (solid.sx, sy and sz).

2.2.1. Material, geometry setups and their limitations

No polymer cladding

This model is only made of a silicon core of 0.22μm height and 0.45μm width. With a silicon dioxide substrate, submerged in water. All mechanical and optical properties were known and were used from the COMSOL material library.

S1805 photo-resist claddings

There are 2 models, one fully coated with 6μm height and one patterned with 0.5μm height and 2μm width. No relevant data was found concerning the mechanical properties of S1805. It's refractive index is assumed to be similar to S1813 which is on average n=1.7 [18]. For the mechanical properties it is also approximated to be similar to S1813 which has a Young's modulus of 22GPa and the poisson's ratio remained unknown so it was given an average value of 0.25 [19]. The stress optic coefficients were not known as well, so the coefficients of BCB polymer were used and modified. Both materials are comparable in terms of elastic modulus and are assumed to have similar strains [20]. To adapt the stress optic coefficients of BCB to S1805, it was assumed that both materials have the same strain but a different stress value, therefore by changing their elastic modulus values in equation 1.22 where $E_{BCB} = 2.9$[GPa] and $E_{S1805} = 22$[GPa], the S1805 coefficients are computed to be $C1_{S1805} = 13.1$[1/TPa] and $C2_{S1805} = 4.1$[1/TPa].

IP-PDMS claddings

Again, there are 2 models, one fully coated with 6μm height and one patterned with 3μm height and 2μm width. The mechanical and optical properties were used from the nanoguide website [21]. It has a refractive index of 1.45, and a young's modulus of 13.5MPa. No poisson's ratio for IP-PDMS was available so the poisson's ratio of PDMS which is 0.48, was used [22]. IP-PDMS and BCB are not comparable material because IP-PDMS is much softer so it was not possible to make any assumptions to obtain . In the literature, there were no found materials with higher stress optic coefficients than BCB as most values were around 1-40 [1/TPa] [20]. For IP-PMDS, it was decided to simply use the stress optic coefficients of BCB. This would provide good sensitivity to stresses but without deviating from common coefficient values because of the uncertainties about its coefficients.

The main limitation of these models is that too many approximations about the materials properties were done. It is not expected that these models can yield accurate quantitative results. Nonetheless, they can still be useful for a qualitative analysis to compare the effect of patterning between the full cladded and pattern cladded polymers.

2.2.2. Conversion of neff sensitivity to pressure, to resonance shift to pressure

Since only the change of n_{eff} with respect to pressure can be obtained with COMSOL, while the pressure induced resonance shift is determined with the optical setup, it is required to convert the COMSOL change of n_{eff} from pressure to its equivalent micro ring resonance shift.

Previously in chapter 1, the MRR equation that relates resonance frequency to the effective refractive index of a waveguide states that:

$$\lambda_{res} = \frac{n_{eff} L}{m} \quad \Delta_{\lambda_{res}} = \frac{\Delta_{n_{eff}} L}{m} \tag{2.7}$$

Since, the waveguide cross section is simulated, the n_{eff} value is obtained. The MRR equation can first be used to determine the mode number m, based on the computed n_{eff} in COMSOL when no pressure is applied.

$$m = \frac{n_{eff0} * L}{\lambda_{res0}} \tag{2.8}$$

Where n_{eff0} is the computed effective refractive with no pressure (from COMSOL), L is the perimeter of the ring and λ_{res0} is the chosen wavelength for computing the simulation. Since m is a mode number, it must be an integer value but because it is not possible to compute the number with full precision, the obtain value must be rounded to the nearest integer. Finally the pressure induced change of n_{eff} can be converted to the pressure induced resonance shift with the equation below.

$$\lambda_{res} = \frac{n_{eff} * L}{m} \text{ thus } \quad \frac{\Delta_{\lambda_{res}}}{\Delta P} = \frac{\Delta_{n_{eff}}}{\Delta P} * \frac{L}{m} \tag{2.9}$$

The model of the ring and its dimensions are taken from a gds file. The length of the ring was computed to be 111.4μm.

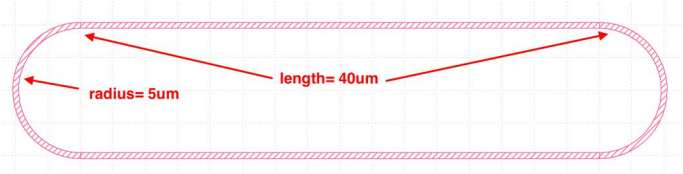

Figure 2.17: Ring dimensions

3

Methods

In this chapter are described several attempted methods of pattern fabrication to make a polymer cladding on top of a silicon chip MRR. In the second section is described the optical-ultrasound characterisation method.

3.1. Fabrication methods

For pattern fabrication, fabrication methods are chosen based on available material and minimum feature size. Feature size is the most important, because sub-micron resolutions are needed to pattern claddings. Concerning material choices, polymers should be used for their softness (especially PDMS), this enhances MRR response to ultrasounds which should facilitate observing the differences of responses between full and patterned claddings. However, if not able to use polymers, other materials such as photo-resists can still be used. The first attempted method was to use a laser cutter as an etching tool. There were no clear indications concerning achievable features sizes when working with PDMS, thus dose tests were made. The second attempted method was to use a laser writer. This is a quick and easy to use method, however it has limited feature size of $1\mu m$ and only photo-resists where available to be used. Finally, the 2 photon polymerization (nanoscribe) was attempted which can produce sub-microns features and can be used with PDMS (IP-PDMS). However, it is quite difficult to work with it, since it has a small printing area of maximum 40x40μm^2, it is also quite sensitive to impurities and alignment can be difficult. Each of these methods has it sets of advantages and drawbacks. From the obtained patterns that will be shown in the results chapter, ultrasound measurements will be conducted with the printed polymer patterns.

3.1.1. Laser cutter

For this fabrication method, a PDMS mixture preparation was made and used to coat diced silicon chips. They will be used with the Lasea laser cutter to determine the best parameters (Power, Speed, Repetitions, De-focus) for making the smallest and cleanest patterns but without cutting through the layer of $Si0_2$. The motivation for using such method is that the laser cutter would be used as an etching tool for removing only the thin PDMS coating. It is simple to use and could be a very fast and effective method if the appropriate laser parameters are found.

The PDMS mixture is summarised as follows:

1. **Preparing silicon chips**: A silicon wafer was diced and cleaned from particles using solvents.
2. **PDMS mixture preparation**: In a plastic falcon dish, 4grams of PDMS with its curing agent where placed in it with a ratio of 10:1 (PDMS, Curing-Agent) using a pipette or wooden stick and were mixed together for 5 minutes.

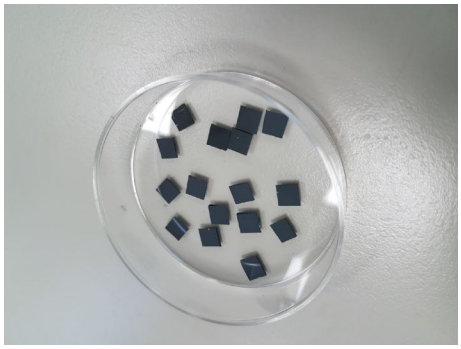

Figure 3.1: Silicon to be coated

3. **Desiccation**: To remove bubbles caused by the mixing of the components, the mixture was put in a desiccator for 30 minutes. This is a crucial step because if there are bubbles left (not visible to the eye), the heat generated from the laser cutter will cause them to pop.

Figure 3.2: Desiccated mixture

4. **Spin coating**: Depending on spin speed, time and the mixing ratio, the thickness will vary. The chips were coated with 2 drops of PDMS mixture all over the region. The parameters used are 6000 rpm with an acceleration of 500, and a time of 180 seconds which should give a thickness of around 5-6μm (see spin-coating chart available in the chemistry lab library). Edge beads were removed with a cotton stick.

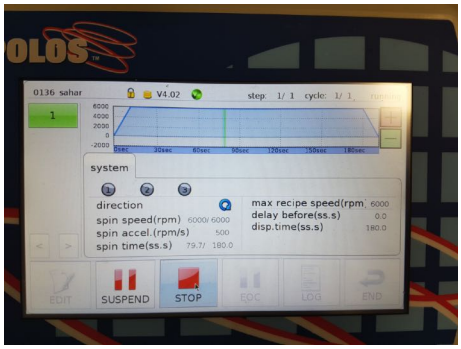

Figure 3.3: Parameter of spin coater

5. **Curing**: The chips were put inside an oven at 80 degrees Celsius for 2 hours.

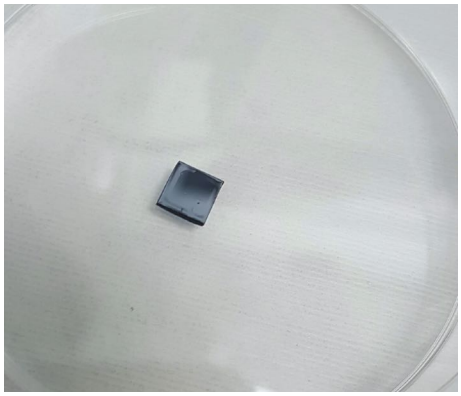

Figure 3.4: Coated silicon

To find the best laser parameters, a total of 5 dose tests were done where in between the tests, the cuts were observed on the microscope to find which parameters had to be changed. On the laser software (Kyla), multiple straight lines of 0.5mm were drawn using parameters matrices where parametric sweeps of speed, power and repetitions were created such that different parameters can be tested in one cutting job.

The 5 dose tests are explained below:

1. The first test was done to approximately find the maximum laser power to be used. Thus a sweep from 5 to 55$\%$ power was done with steps of 5.
2. In the second test, speeds were compared to determine what is the maximum speed that could be used while still having straight lines. It should be noted that, as the cut is finer, deviations in the cutting path are more noticeable.
3. Following the 2 previous tests, in the third experiment, sweeps of power from 1 to 6$\%$ were done to test even lower powers in order to reduce cut widths. When focused with power of 1$\%$, it is still cutting through the PDMS. It is likely that the surface of the silicon was reached.
4. Burnt edge thickness were still too large despite having used the minimum power of 1$\%$ so to prevent those, in the 4th experiment, while still using a power of 1$\%$, a de-focus was done to make the surface area larger and spread the energy more in the area. This should make the cut larger while reducing the burnt edges. Having larger cut widths were not a concern because they can be offseted later on. However, the cuts shapes and amount of PDMS were not even, so an additional experiment was done.
5. In the 5th and final experiment, repetition sweeps with different de-focus and repetitions were done to attempt to control the amount of the PDMS removed and improve the cut shapes. The combination of these 2 sweeps, allowed to control more or less the amount of PDMS removed. However the cutting was still not consistent in many instances.

3.1.2. Laser writer

In a previous experiment it was attempted to make geometry patterns on a PDMS coated silicon chip using a laser cutter. Unfortunately, it was not successful as the laser power was too high (even when using the lowest amount of power) which caused large brown edges. Another option available was to use a laser writer that can make smaller feature sizes of around 1μm. Unfortunately, the geometry pattern can only be applied to a photo-resist which is not as soft as PDMS but it can be easily removed with acetone which was worth trying.

Laser writing

First, the choice of photo-resist is S1813 (1.4μm thick) and S1805 (0.5μm thick) which are often used in the Clean-room lab. They are positive resists, so the boolean of the desired geometry was made to be used as the pattern for the laser writer. The writing device is the MLA 150 which is a mask-less lithography machine that is used for the exposure step of the lithography process. The laser pattern

is created in a Spatial light modulator (SLM) which is a transparent screen in which the laser light goes only through the pattern. This light then goes through a mirror and focusing lenses to expose the chip to the patterned laser light. It has a minimum feature size of 1μm, alignment accuracy of 500nm and operates with UV wavelengths of 375 and 405nm [23]. Depending on the size of the chip and the wavelength, the photo-resit is cured from 4 to 36minutes. The chip can then be developed in a solution.

Mask design

To produce the mask, KLAYOUT and the GDSFactory python library were used. Using the Master GDS file from Dr. W.Westerveld's photonic chip from his PhD, 2 MRR device groups were chosen based on their good optical coupling efficiency.

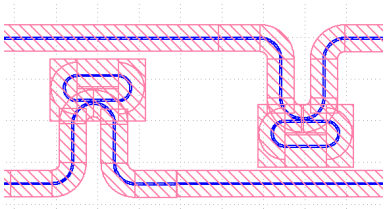

Figure 3.5: MRR named ww-smallrr-R3

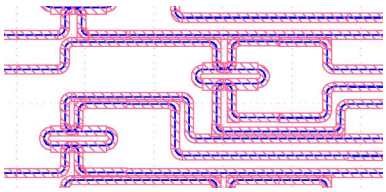

Figure 3.6: Add drop MRR named ww-dcring-w450-g200

Then using the extracted geometries, a python code was made to generate a .gds and .stl file of the masks with different cladding widths. The code design process is described as follows:

1. From the master GDS of the photonic ship, the MRR device regions were copied and pasted into a separate .gds file. In addition, another file was made to include the markers from the chip to align the laser writer mask with the chip.
2. The device regions were modified to fill the coupling region between the bus waveguide and the ring. The purpose of this, is to remove the acute angle which cannot be reproduced accurately because the feature size would be extremely small and cannot be produced by the laser writer.

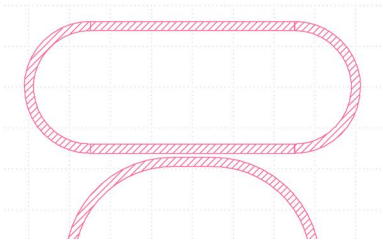

Figure 3.7: Unfilled gap

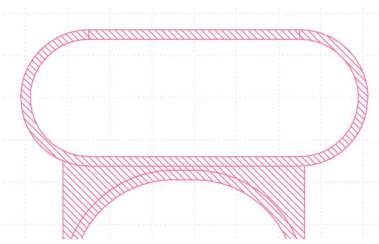

Figure 3.8: Filled gap

3. On python, the .gds files of the modified MRR were imported into separate components.
4. The gf.geometry.invert command was used to create the boolean of the geometry with a bounding box border of 15μm.
5. An gf.geometry.offset command was used to change the cladding widths of the booleans.

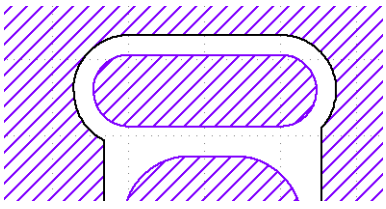

Figure 3.9: Resulting shape of MRR

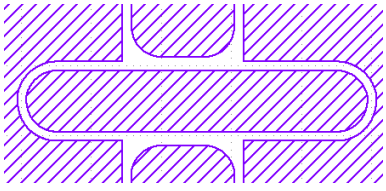

Figure 3.10: Resulting shape of Add-Drop MRR

6. Markers as well as the original waveguide cores were included to the offset-ed components with different cell names. They cannot be with the same cell name, otherwise the markers would also be printed.
7. A .gds file to .stl file converter option was included if the user wishes to get the stl file as well.
8. The previous 3 steps were used in a 'for' loop to automate and export .gds and .stl files with different cladding widths all at once.

The files mask files were given to PhD candidate Paulina C. Rodríguez who kindly accepted to do the laser writing since the Cleanroom access is usually not given to MSc students. A dose test was conducted by her to ensure that small spacing gaps between features would not cause print defects. A parametric sweep of spacing from 0 to 4μm was done with gaps of 0.25μm.

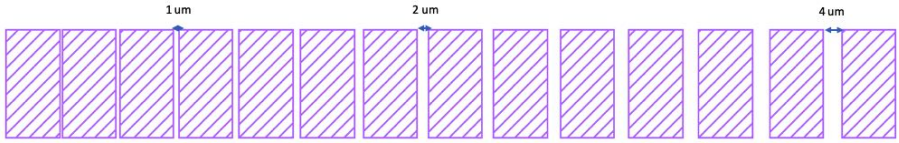

Figure 3.11: Dose test sweep of spacing gaps

3.1.3. Nanoscribe

The nanoscribe is a device that does a two-photon polymerization (2PP) which is a 3D printing technique used to make micro and nano-structures. It relies on the simultaneous absorption of two photons by a photo-polymerizable material, typically a photosensitive resin to initiate polymerization. The 3D patterning is made by moving the laser focus point where the polymerization occurs [24]. The steps taken to print a pattern on a substrate are explained below.

1. Import a .stl file geometry into DeScribe software to slice and hatch the model and setup the job file with appropriate laser parameters (multiple models with different parameters can be printed to do a dose test.)
2. Choose a substrate material and the x63 objective, and clean them with PGMEA and IPA. There should be no visible impurities otherwise the interface might not be found. Place the objective in the nanoscribe
3. Fix the substrate to the substrate holder and put 2 drops of resins on it and place it upside down in the nanoscribe.
4. Do an interface search and if not found, change piezo position or amplitude threshold.
5. Load the job file and print

Cladding patterns were made using IP-PDMS and IP-Dip2 that can achieve very small features compared to IP-PDMS. Both were tested on fused silica, silicon and ITO (Indium tin Oxide) coated fused silica. The goal was to use IP-PDMS because of its softness, and works the best for medium feature sizes of average 10μm and with the x25 objective. IP-PDMS does not work well with the x63 objective and it has never been attempted to find a solution to that problem. To tackle this problem, multiple dose tests were done by printing lines of 10μm length, 1.2μm width, 1.4μm thick with sweeps of power and speed. In addition, sweeps of depths of prints in the substrate were done to help the printed structures adhere better to the substrate. The default value of depth was 0.5μm and was kept that way so the resulting height of the line was (1.4-0.5μm=0.9μm). For the IP-Dip2, a similar dose test was done to compare experiments. For IP-Dip2, the speed and power were slightly adjusted to have better line shapes in case they were not perfectly straight. Different hatching and slicing sizes were tested as well with size from 0.1 to 0.5μm. Following the dose tests, a dummy chip (with unusable devices) was used to test printed patterns on it with the 2 mentioned resins. The determined optimal values from the dose tests with silicon and glass were not quite adapted, so a dose test was done directly on the chip. This is caused by the fact that the chip is glued to a substrate so there is a small tilting. And in addition, the chip surface is not uniform because of the waveguide structures. In this case, the interface should be

found manually to have a better quality of prints and not have to increase laser power to compensate for tiny mismatches between the real and found interfaces (in other words a slight de-focus).

Finally, to do an alignment since the printing region is very small, it was not possible to align with the markers of the chip. The chip does not always have the right rotation so when printing a pattern, the print is always with a rotation offset. However, a solution was found for these problems which requires few steps.

1. From the Nanowrite software camera view, place 2 markers point on the screen that are on a x axis on the chip. These are called real points, then for each marker point, define a design marker point to make the equivalence between the coordinates of the chips and the camera coordinates. This will align the X axis of both the chip and the camera which removes the rotation offset.
2. On a empty space on the chip, far from devices, print a first pattern and set camera blue cursors such that each cursors axis are at the middle of the width axis as shown below:

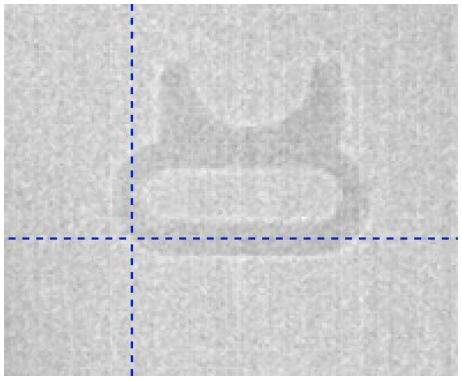

Figure 3.12: Cursor positioning

3. With the piezo stage move to the desired device while keeping the cursor at the same position, and position the chip such that the cursors axis are the middle of the waveguide widths.

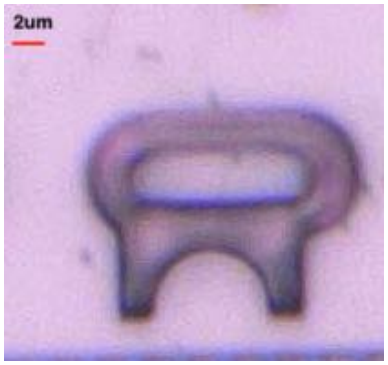

Figure 3.13: Made ring pattern (Microscope view)

Finally, to remove printed IP-PMDS from a MRR to be able to reuse it, a PGMEA/TBAF solution with 1% weight of TBAF was used. The silicon chip was put inside the solution container, in an ultrasonic cleaner bath heated at 50degC. It must sit there for 3 minutes and an additional 2 minutes could be added while using the ultrasonic cleaning (delicate mode).

3.2. Optical ultrasound characterisation

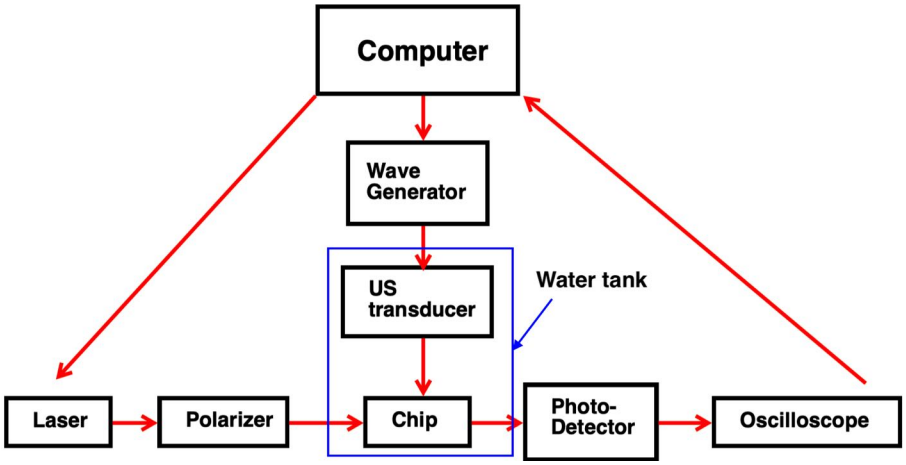

Figure 3.14: US setup Schematic

The measurement setup works as such: A laser light is generated by a variable wavelength laser that goes through a polarisation controller and to a fiber tip which is coupled to the grating coupler of the MRR device. At the other end of the MRR waveguide is another fiber coupled that is connected to a photo-detector. A DC signal is generated and is used to adjust the fibers and couple them, and an AC signal is used to measure the sensor's response to the incoming ultrasound signal. The ultrasound transducer is placed inside the water tank on top of the chip at around 3.6cm, and is connected to a waveform generator which generates a pulse signal. To do an optical measurement, a wavelength sweep is done to characterise the MRR and determine its different resonance frequencies. Once determined, the resonance peak with the highest slope of intensity with respect to wavelength is selected because it is the most sensitive. It should be noted that the wavelength is +0.15nm longer in the setup than in real life, this was noticed by Tufan. The laser wavelength is changed to the corresponding wavelength of the highest slope (flank wavelength), and the coupling voltage efficiency will be dropped by approximately half of its initial value. On the waveform generator, a trigger is set up to the oscilloscope to tell when to start recording, otherwise it will not be possible to tell at which time the US wave can be seen. A python code is run to conduct the measurement and record data as a hdf5 file.

Every ultrasound measurement must be done with the same positioning and conditions to ensure consistency of results. The distance between the US transducer and chip should be around 3.6cm which means that the time for US wave to travel from the transducer to the MRR, will be 24us (assuming a 1500m/s sound speed in water). For every measurements, the transducer height must be adjusted such that the US wave starts at 24us. To determine how much pressure is at the chip, the pressure was measured between the US transducer and a pressure sensor to determine a conversion ratio between the input US peak to peak voltage (V_{pp}) and the pressure at the chip surface. This voltage to pressure conversion ratio was measured by T.Erdogan with a calibrated hydrophone and determined to be 2.76 kPa/V_{pp}. This way the output peak voltage can be converted to its equivalent pressure and will be used to determine the sensitivity to pressure.

The highest peak voltage of the time signal is recorded for a set of input voltages from 0 to 5V. The peak voltage is converted to pressure and a graph with its fitted line is generated. The slope of the fit will be the pressure to input voltage sensitivity The input "peak to peak" voltage conversion to pressure is written as:

$$P = V_{pp} * P_{conv}[kPa] \tag{3.1}$$

Where V_{pp} is the input peak to peak voltage of the waveform generator connected to ultrasound transducer, V_{peak} is the maximum measured peak of the AC signal according to each V_{pp} and P_{conv} is the voltage to pressure conversion constant. The peak voltage sensitivity to pressure is written as:

$$\frac{dV_{peak}}{dP} = \frac{dV_{peak}}{dV_{pp}} \div P_{conv} \tag{3.2}$$

To determine the resonance shift from pressure, first, the response of the device at different wavelengths is measured (figure 3.15). Then the slope of this measurement is calculated after filtering the received signal (see figure 3.17). The minimum point of this measurement gives the $\partial V_{peak}/\partial \lambda_{flank}$ calculated at the flank wavelength (figure 3.16).

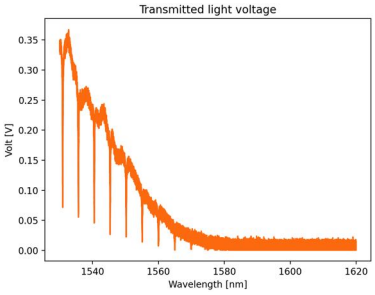

Figure 3.15: Wavelength sweep

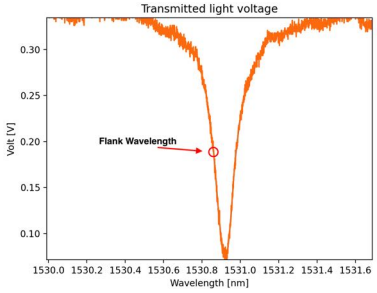

Figure 3.16: Flank wavelength from 1st resonance peak

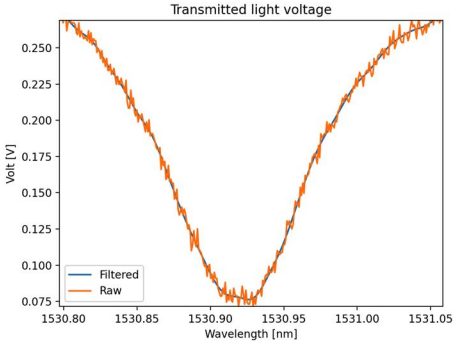

Figure 3.17: Raw vs Filtered data with low pass at f=2k

Then the ultrasound transducer is aligned to the MRR resonator, and a sweep of wavelengths close to the resonance frequency is done while recording the sensors response to find the optimal flank wavelength value. After this procedure, the sensors' response is recorded with different pressure pulse amplitudes (figure 3.18). The slope of this measurement will give the $\partial V_{peak}/\partial V_{pp}$.

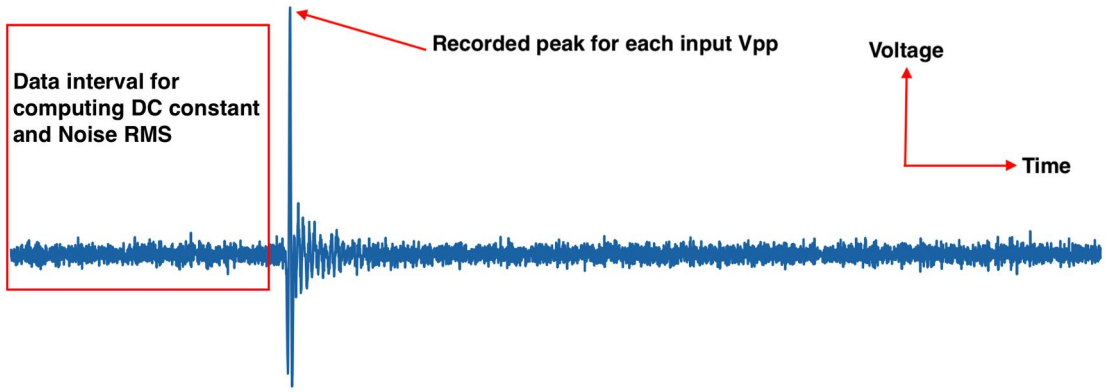

Figure 3.18: Voltage (AC) signal over time

Dividing $\partial V_{peak}/\partial V_{pp}$ to $\partial V_{peak}/\partial \lambda_{flank}$ will give $\partial \lambda_{flank}/\partial V_{pp}$ which can be calibrated with a calibration factor P_{conv}. Hence is obtained $d\lambda/dP$ [fm/kPa]

$$\frac{d\lambda_{flank}}{dP} = \frac{\partial V_{Peak}}{\partial V_{pp} * P_{conv}} \div \frac{\partial V_{Peak}}{\partial \lambda_{flank}} \tag{3.3}$$

With the determined wavelength shift from pressure, the limit of detection (LOD) can be computed.

$$LOD[kPa] = \frac{\Delta\lambda_{noise}}{dS} \tag{3.4}$$

Where $\Delta\lambda_{noise}$ is wavelength shift from noise (without averaging), S is the wavelength shift to pressure.

3.3. Data acquisition and analysis

In the ultrasound measurement python code, the measurement procedure is summarised below:

1. Doing a frequency sweep to obtain the intensity spectrum
2. Search for the slope at the resonance wavelength (flank wavelength) from the spectrum. Then step-scan at the vicinity of the flank of the resonance to determine accurately the best wavelength to operate.
3. Record the AC signal at the flank wavelength and with a parametric sweep of the input voltage V_{pp}, record the sensor response for different pressure amplitudes of ultrasound pulses.
4. Measure noise levels ON the flank wavelength
5. Measure noise levels OFF the flank wavelength

During the data acquisition of the AC voltage (volt over time), for each V_{pp} value, the average of 1000 measurements was taken to reduce the noise effect. The photo-detector has different gain values between the channels of AC (40V gain) and DC (10V gain), thus for computing the sensitivities, the voltage values of the frequency sweep spectrum which were measured with the DC channel were multiplied by a factor of 4. For the acquired AC signal, there is a constant DC bias signal which means that for a $0V_{pp}$ input voltage, the output voltage is not zero which will change the sensitivity slope values if not removed. Therefore, an average of the AC signal was computed which gives the DC bias and was deduced directly from the AC signal. After removing the DC bias, the noise rms is determined from the signal. The root mean square (rms) is measured in a time interval that starts at time equals to 0 and ends before the wave peak signal arrives. This is to avoid getting wrong rms values because of the wave peak and other peaks from reflections. From the AC data with removed DC bias, the corresponding V_{peak} for each input V_{pp} is measured. Because of noise, errors will be contained within the peak values.

The measured peaks are composed of the signal amplitude and random noise:

$$M = A + N \tag{3.5}$$

Where M is the measured signal, A is the signal amplitude and N is the noise. By taking the average of M^2, the average of the noise squared is the noise rms squared. Since A and N are uncorrelated, the average of $2 * A * N$ is zero

$$M^2 = A^2 + N^2 + 2 * A * N \tag{3.6}$$

$$M_{avg}^2 = A_{avg}^2 + N_{rms}^2 + 2 * A_{avg} * Navg \tag{3.7}$$

Then:

$$M_{avg}^2 = A_{avg}^2 + N_{rms}^2 \tag{3.8}$$

$$M_{avg} = \sqrt{A_{avg}^2 + N_{rms}^2} \tag{3.9}$$

The figure below assumes a 4mV noise rms and computes the M_{avg} starting at 0 input peak A, to visualize how the curve would look like from the US measurements that will be done.

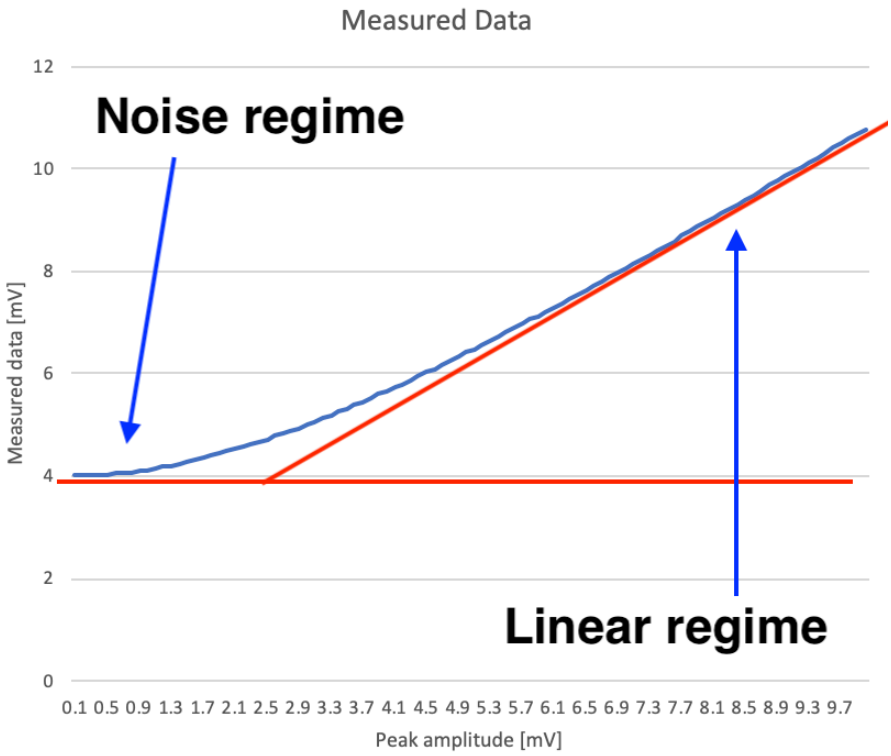

Figure 3.19: Linear and noise dominated regimes

The input V_{pp} voltage was converted to its equivalent pressure with P_{conv} from equation 3.1 to determine the slope of the peak voltage to pressure. The slope were obtained by making fitted lines of the data. The first fit was a quadratic fit, which gives a fitted line in the form of $y = ax^2 + bx + c$. This fitted line is meant to fit both the low input V_{pp} that would be dominated by noise and would be more or less constant and at high V_{pp} which should be linear as peaks values would gradually increase (see figure 3.19. Another fit to consider is a linear fit that starts from the origin, without the presence of noise, a 0 input V_{pp} would give a 0 output V_{peak}. This would happen when noise noise exists (ideal scenario). A linear fit in the form of $y = ax$ can be used to have a fitted line that starts from the origin point (0,0) to compare with the quadratic fit when sensitivity is high and see how the quadratic fit compares with the ideal scenario. Both these fits could be feasible and will be used and compared to the raw data together in one graph with the measured peaks (and peak error bars).

Using the slope at the flank wavelength (written as $dV_{peak}/d\lambda$) and using the slopes from the 2 fit types made from the V_{peak} to pressure graph (written as dV_{peak}/dP), the pressure induced resonance shifts can be computed.

4

Results

4.1. FEM simulations

In this section, will be given the key values of the COMSOL simulations such as n_{eff}, mode shape number ”m”, n_{eff} sensitivity to pressure and its equivalent pressure induced resonance shift. For each simulation, a graph of the relative change of refractive index in the x and y directions from photo-elasticity is given (at 5kPa pressure). This is to observe where photo-elasticity occurs with respect to the location of high electric fields of the TE mode (figure 4.1). It should be noted that photo-elasticity is not observable on optical setup. Figure 4.1 shows the high electric field location for the patterned S1805. Compared to the other cladding configurations, differences of location are very negligible so it is not required to show their plots again and figure 4.1 can be compared with all (n_x-n_y) graphs. Each model was simulated using a wavelength of 1.55μm. The sensitivity $\Delta n_{eff}/\Delta P$ was determined by plotting each respective of n_{eff} with its applied pressure (sweep from 0-5kPa). The m mode shape values were calculated from the determined n_{eff} value when no pressure was applied and with a MRR length of $L = 111.4\mu m$. Finally, the resonance shift was calculated using equation 2.9.

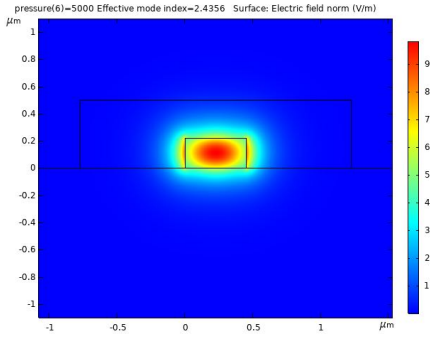

Figure 4.1: TE electric field plot of patterned S1805

No cladding

With no cladding, the computed n_{eff} (without pressure) was 2.3564, m number was 169.0 with a sensitivity of -4e-12 [1/Pa]. The equivalent resonance shift was computed to be -2.637e-06 [nm/kPa].

S1805 no pattern and patterned cladding

With a full coat S1805, the computed n_{eff} was 2.4356, m number was 175.0 with a sensitivity of -4.371e-12 [1/Pa]. The equivalent resonance shift was computed to be -2.783e-06 [nm/kPa].

With a patterned S1805, the computed n_{eff} from COMSOL was 2.4356, m number was 175.0 with a sensitivity of -1.3629e-11 [1/Pa]. The equivalent resonance shift was computed to be -8.677e-06 [nm/kPa]. The gradient colours of the graphs below show n_x-n_y.

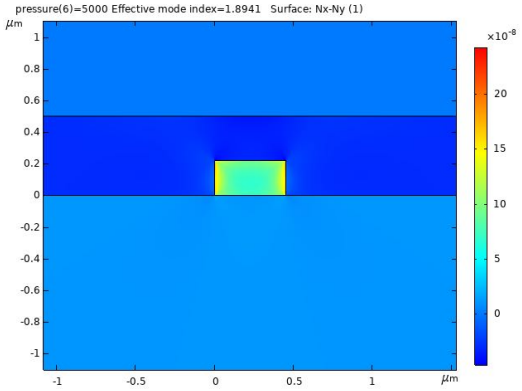

Figure 4.2: No pattern S1805

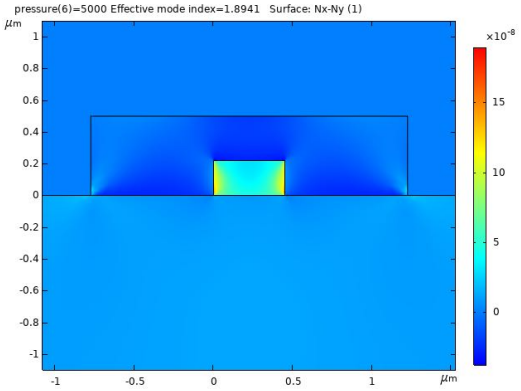

Figure 4.3: Patterned S1805

IP-PDMS no pattern and patterned cladding

With a full coat IP-PDMS, the computed n_{eff} was 2.3802, m number was 171.0 with a sensitivity of 1.0286e-11 [1/Pa]. The equivalent resonance shift was computed to be 6.702e-06 [nm/kPa].

With Patterned IP-PDMS, the computed n_{eff} was 2.3802, m number was 171.0 with a sensitivity of 2.2143e-11 [1/Pa]. The equivalent resonance shift was computed to be 14.427e-06 [nm/kPa].

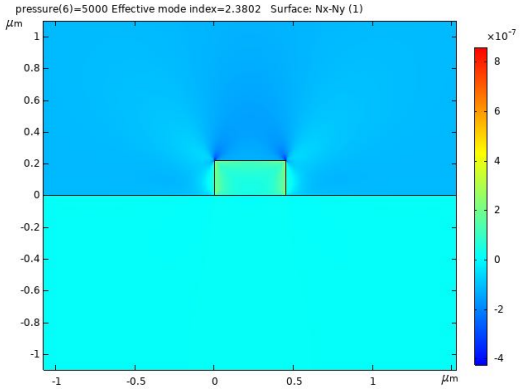

Figure 4.4: No pattern IP-PDMS

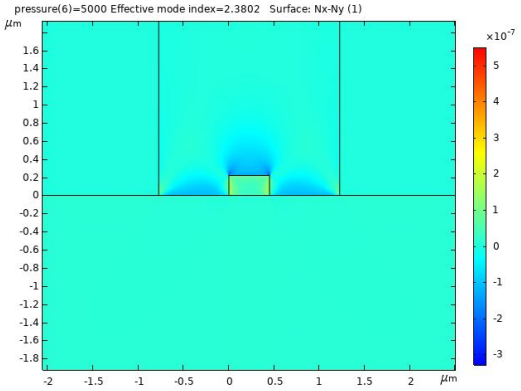

Figure 4.5: Patterned IP-PDMS

Cladding	Resonance shift [fm/kPa]
No cladding	-2.6
Full S1805	-2.8
Patterned S1805	-8.7
Full IP-PDMS	-6.7
Patterned IP-PDMS	-14.4

Table 4.1: Summary of COMSOL sensitivities

4.2. Pattern fabrication methods

In this section, will be shown results and pictures of the different attempted fabrications methods. It will be explained what went right or wrong during the fabrication processes, including relevant pictures for illustration.

4.2.1. Laser cutter

In the first dose test in figure 4.6, for powers over 5%, there was excessive splashing and cuts were too thick.

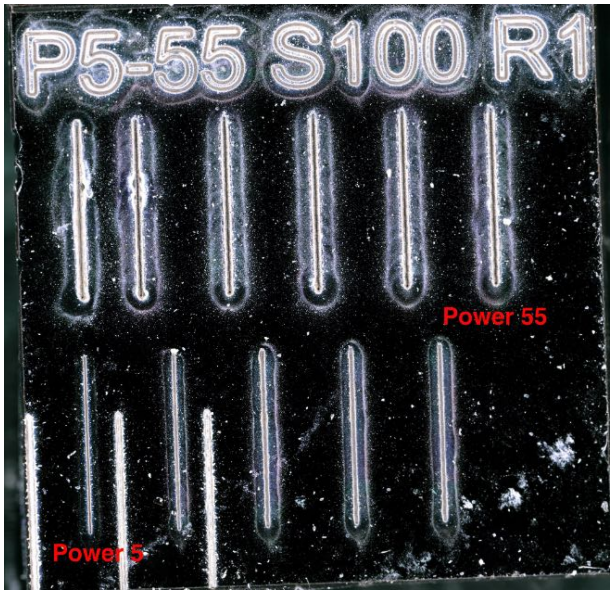

Figure 4.6: Power sweep from 5 to 55 Repetition of 1 and Speed of 100

In the second dose test in figure 4.7, with a constant power of 4% and repetition of 1, it was found that at a speed of 50, lines were not cut through and at a speed of 30, lines were cut through but had path deviations as cuts were finer so the deviations were more noticeable. Thus the power had to be reduced even more.

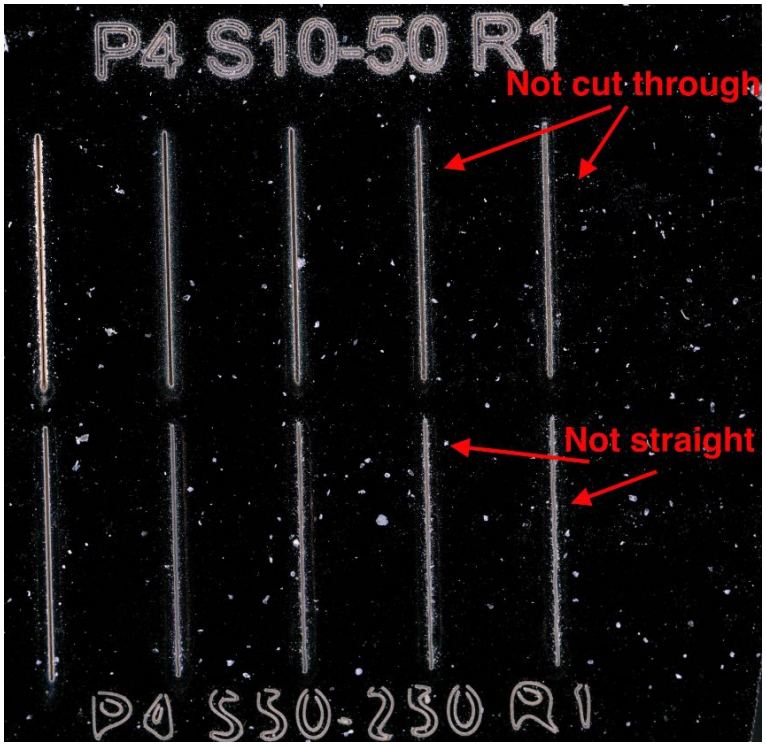

Figure 4.7: Speed sweep from 50 to 250 at bottom lines and 10 to 50 at top lines. Repetition of 1 and Power of 4

In the third dose test in figure 4.8, it was observed that a cut with power 1% gave an even finer width, however the brown edge surrounding region was still too large at around 30μm.

When focused with power of 1%, it was still cutting through the PDMS. It is likely that the surface of the silicon was reached.

Figure 4.8: Power sweep from 1-6%

In the fourth dose test in figure 4.9 and 4.10, when using different de-focus values, the brown edges were significantly reduced but still present. However, line cuts were not consistent because the speed was too high.

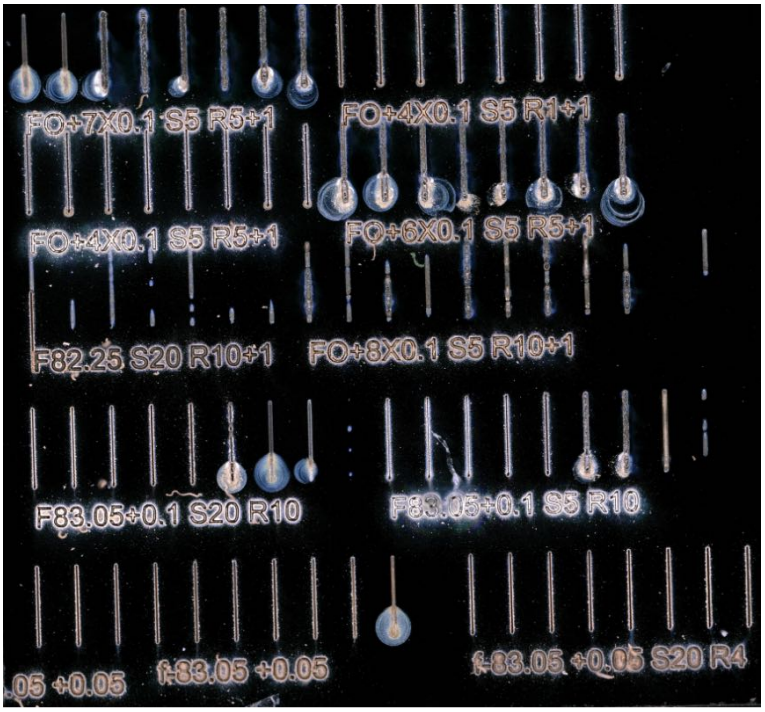

Figure 4.9: Sweeps of defocus

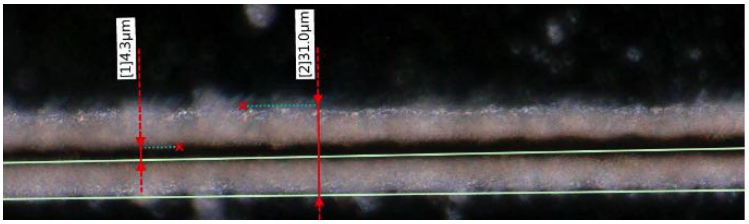

Figure 4.10: focused

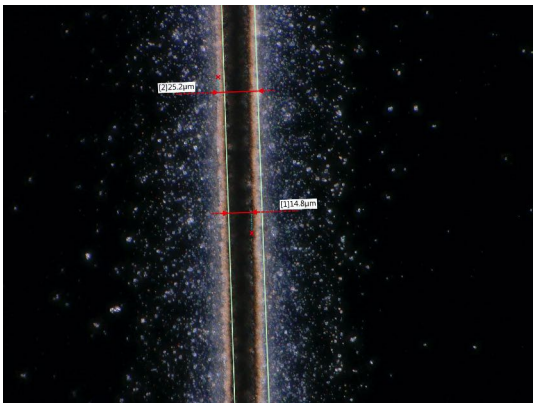

Figure 4.11: Defocused

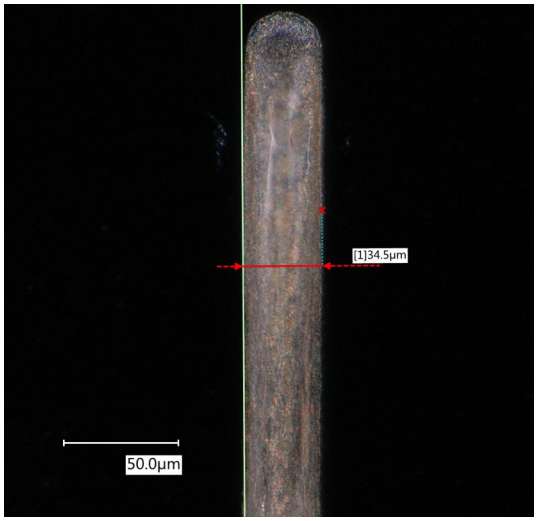

Figure 4.12: Defocused with faster speed

In the fifth dose test in figure 4.13, a sweep of de-focus and repetitions was done to find the best parameter for having more consistent cuts to not have differences in the amount of removed material. However, there were not sufficient improvements compared to the 4th dose test and the limits of the Lasea laser cutter were reached because the power could not be reduced further than 1%.

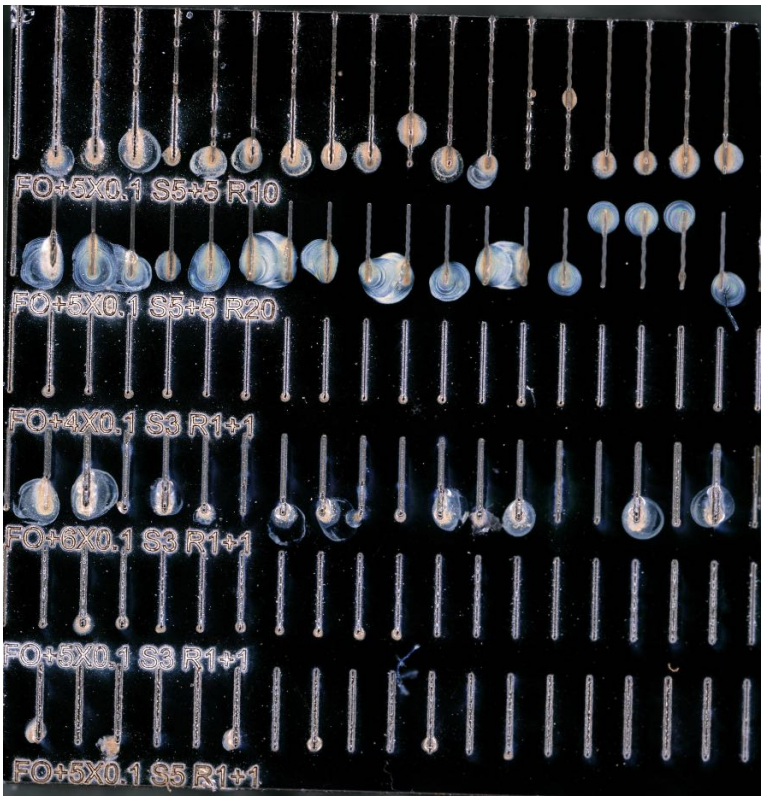

Figure 4.13: Sweeps of de-focus and repetitions

4.2.2. Laser writer

For the first laser writing attempt, S1813 photo-resist was used to print the pattern with a width of $1\mu m$. The dose test showed that using a $1\mu m$ distance between features was at the limit before having features with wrong edge pattern but $1.5\mu m$ would have been safer. For the printed MRR in figure 4.15,

a misalignment occurred which made the print not sufficiently satisfying for doing an ultrasound measurement. An alignment check was done using AFM with the Nanosurf Nanite B. The image resolution was not sufficiently accurate and the positioning of the chip with the AFM tip using bare hands was really difficult for positioning the tip at the desired location. Thus, SEM images were taken instead and gave much better pictures. Looking at the ring core, only a small portion of the printed pattern was on the top of the ring.

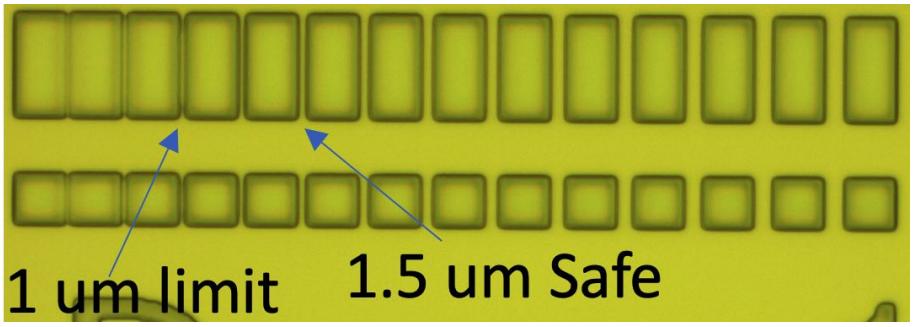

Figure 4.14: S1813 dose test

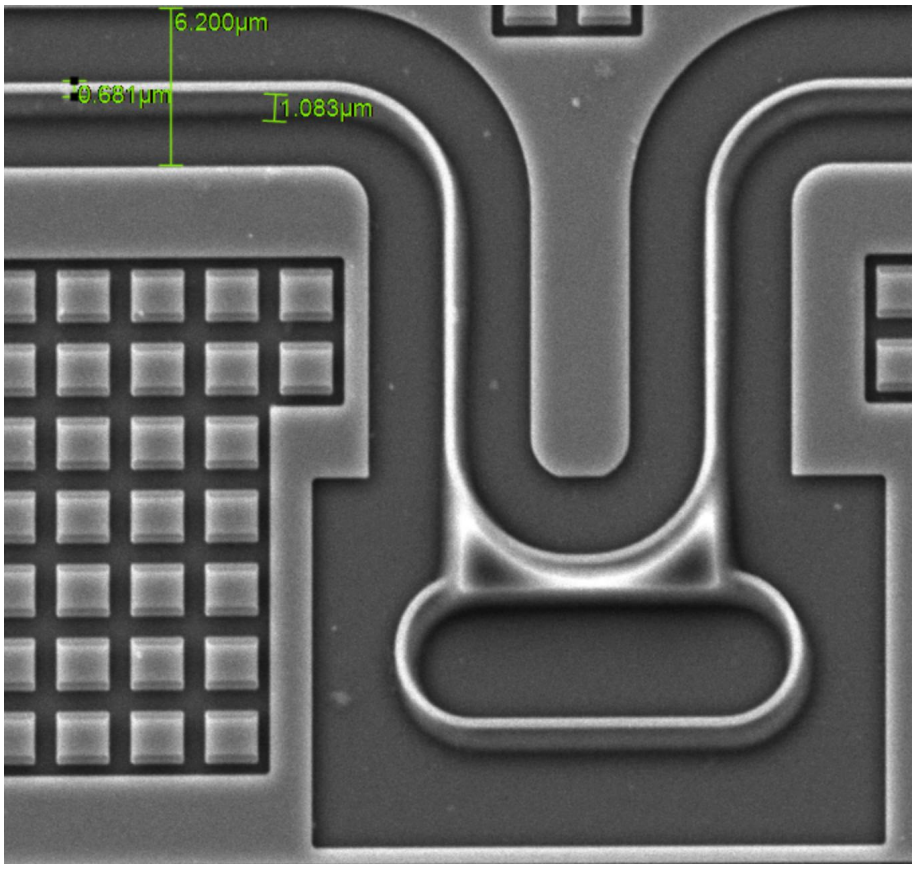

Figure 4.15: SEM alignment measurements

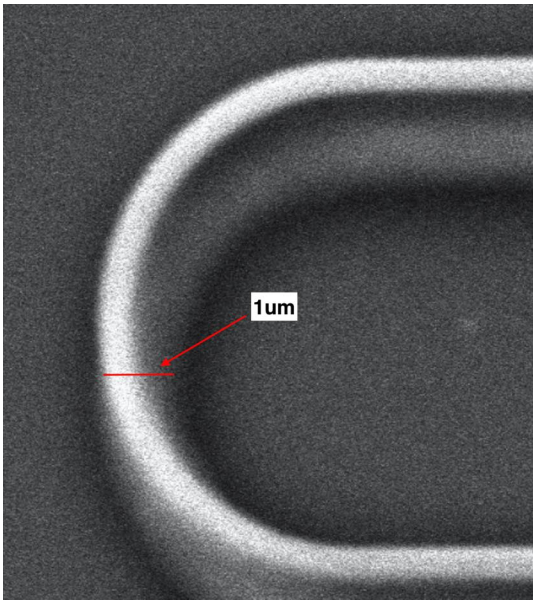

Figure 4.16: Zoomed figure 4.15

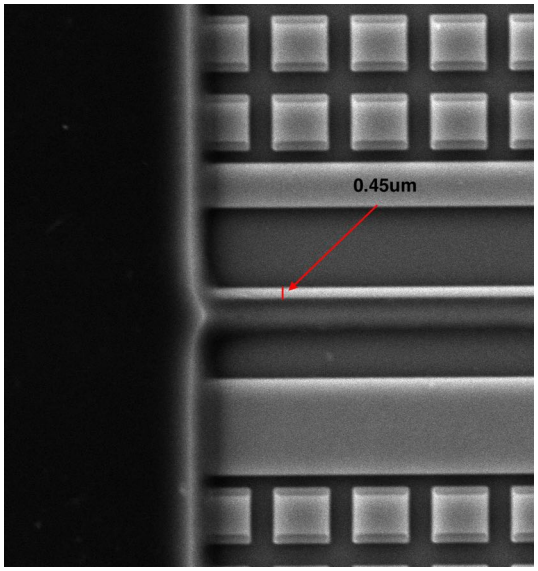

Figure 4.17: Zoomed figure 4.15

In the second attempt, S1805 was used with a cladding width of $2\mu m$ rather than $1\mu m$ to increase chances of having the ring fully covered by the pattern (even if not perfectly aligned). The dose test showed that a $1\mu m$ distance between features was safe and edges were produced accurately. For the printed MRR, there was still a misalignment as it can be seen in the figure below. Since, only PhD student Paulina could access the laser writer, it was not possible to investigate reasons behind this misalignment. Though according to the data sheet of the laser writer the alignment has an accuracy of 500nm. Therefore, it was decided to do an ultrasound measurement with this cladding, rather then pattern it again.

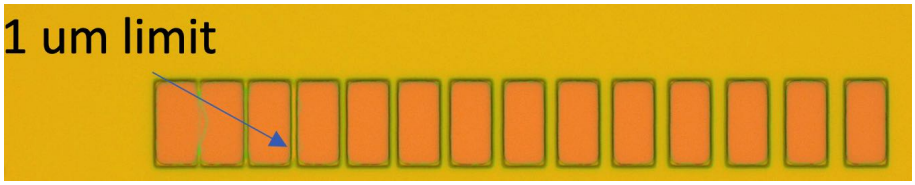

Figure 4.18: S1805 dose test

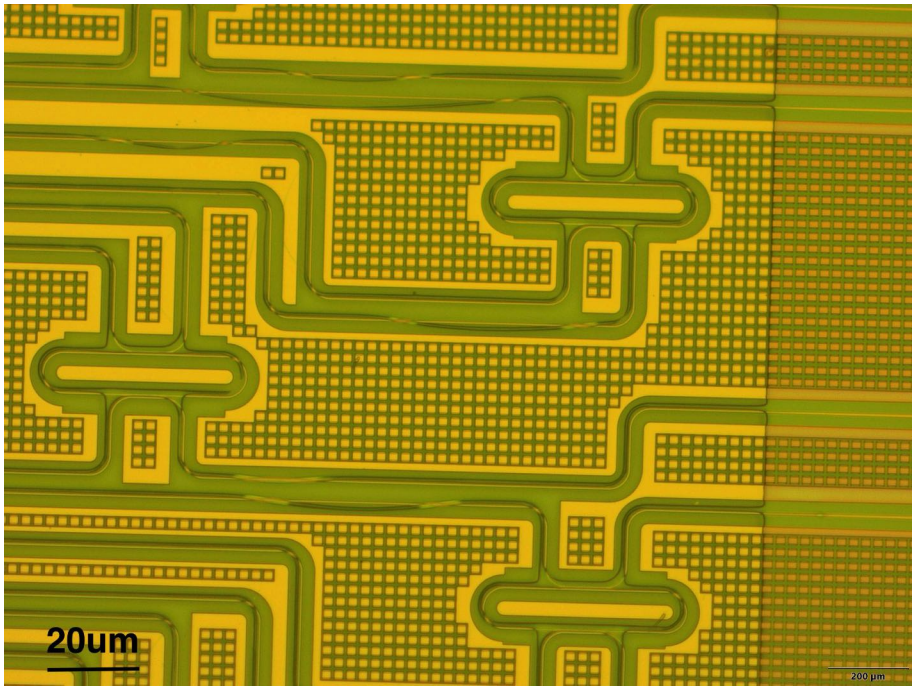

Figure 4.19: Alignment check from laser writer camera

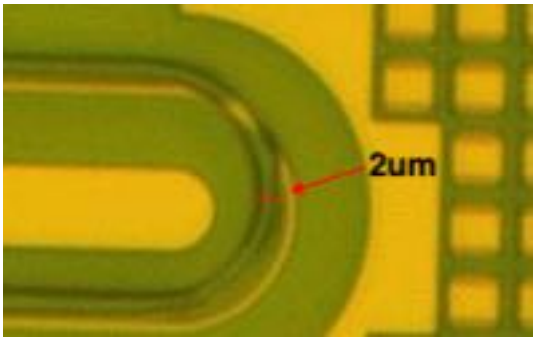

Figure 4.20: Zoomed figure 4.19

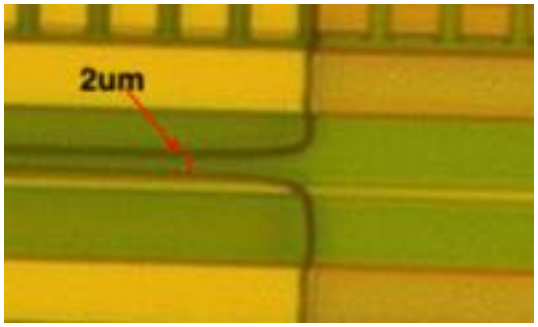

Figure 4.21: Zoomed figure 4.19

4.2.3. Nanoscribe

In this section, results of some dose tests are presented first with test prints on different substrates. Then will be given the results of printed IP-PDMS on a MRR. The experience gained from these test prints led to overcoming many limitations of the nanoscribe and eventually be able to print patterned IP-PDMS with a satisfying feature size on the MRR which has never been done before.

IP-PDMS

First, by using the x25 objective, IP-PDMS was able to work with Silicon and ITO glass and for the x63 objective it worked only with ITO glass. From there, a dose test was done and the best parameters found were using a speed of 1K, a laser power of 100 with amplification factor of 1.2 so 120 power and a print depth of 0.2μm.

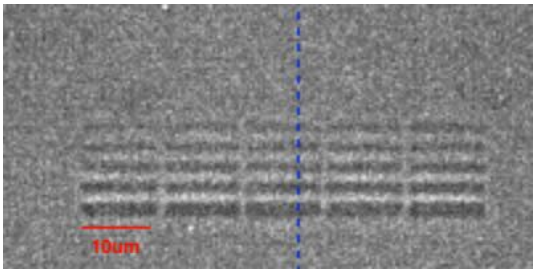

Figure 4.22: Dose test lines (camera view)

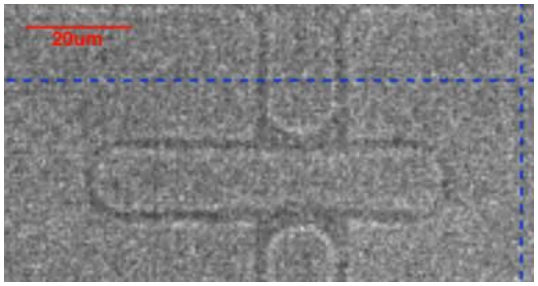

Figure 4.23: Printed pattern (camera view)

After developing the printed structure in isopropanol for 5min to remove uncured resin, the structures became different. The width was expected to be around 1μm but instead it was 3.2μm, which caused some lines to touch while they were supposed to be separate. The main reason for this are the edge bumps which are regions between the edge and substrate where a smooth transition occurs between the top surface of the print and the substrate instead of a sharp transition which was expected. These edges bumps occurred either during the printing or development process but it was not clear which one it was since on the nanoscribe camera, the structure could not be seen clearly.

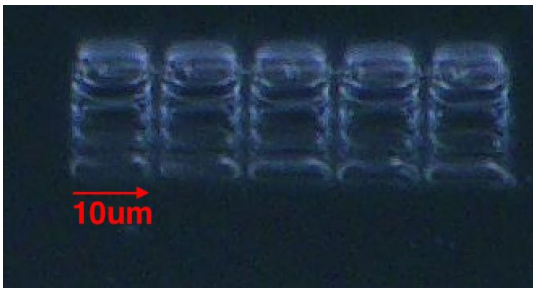

Figure 4.24: Dose test lines (microscope view)

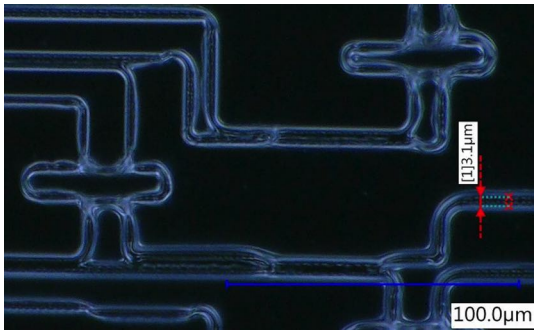

Figure 4.25: Printed pattern (microscope view)

IP-Dip2

The Ip-Dip2 resin was used directly with the x63 with the default laser power parameter from a nanoscribe preset. The best parameters from the dose test were a laser power of 35, a speed of 3K and a print depth of 0.3μm. The printing process was much more stable and consistent even with different laser parameters. Following that, a development in PGMEA for 12min was done and the edges of the print remained clear and sharp unlike with IP-PDMS.

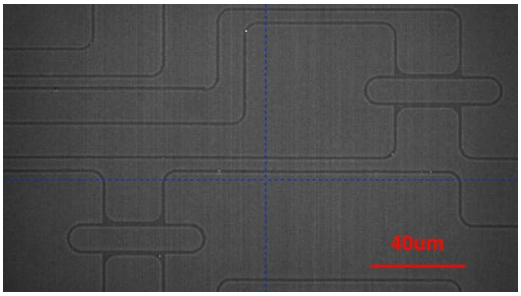

Figure 4.26: Ip-Dip2 on Silicon (Camera view)

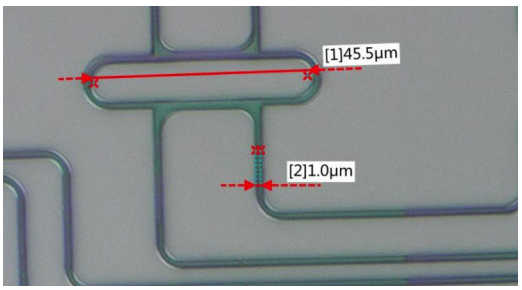

Figure 4.27: Ip-Dip2 on Silicon (microscope view)

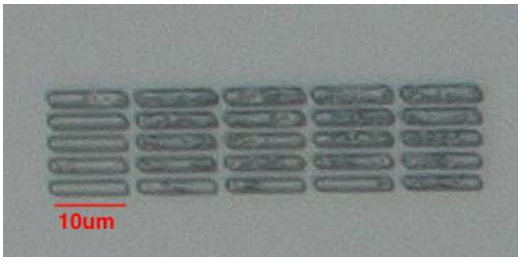

Figure 4.28: Ip-Dip2 on glass (Miscroscope view)

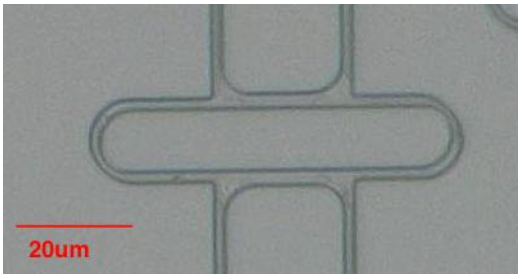

Figure 4.29: Ip-Dip2 on glass (Microscope view)

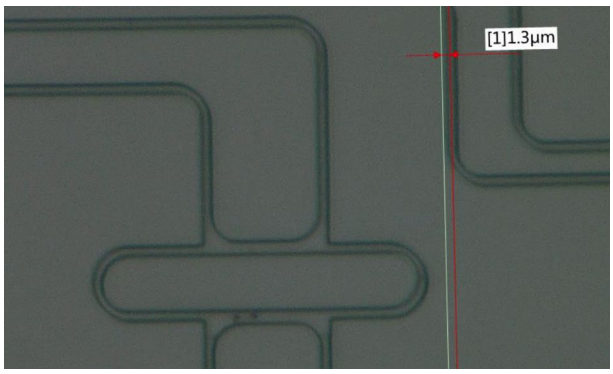

Figure 4.30: IP-Dip2 on glass with 0.2μm slicing, 0.3μm hatching

Following the tests on different material substrates, below are tests done on the dummy chip. Despite the fact that when using the x63 objective, IP-PDMS was not produced accurately as seen on figure 4.25, when printing on the dummy photonic chip, the interface was found easily and the PDMS print took hold quite well. The ring alignment positioning was accurate enough despite a low resolution of the camera. The interface plays a big role in the quality of the print and in this case the interface was found very easily because the substrate was not transparent and waveguide structures contrasted well. With transparent substrates, it often occurs that the nanoscribe finds the wrong interfaces when using the automatic interface finder. Prints will be done with a de-focus or would not appear at all. It is best to first find the interface manually with the z axis knob and then use the automatic search for increased focus.

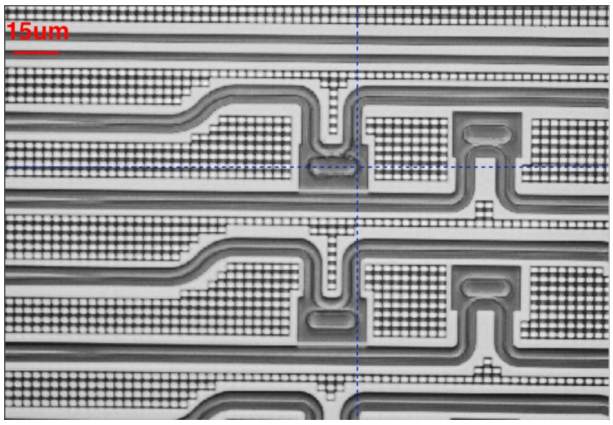

Figure 4.31: Aligned ring

When printing the pattern with PDMS, some edge bumps occurred which made the contrast between the print edges and substrate less noticeable. Finding the right amount of power and speed was quite tricky to reduce edge bumps.

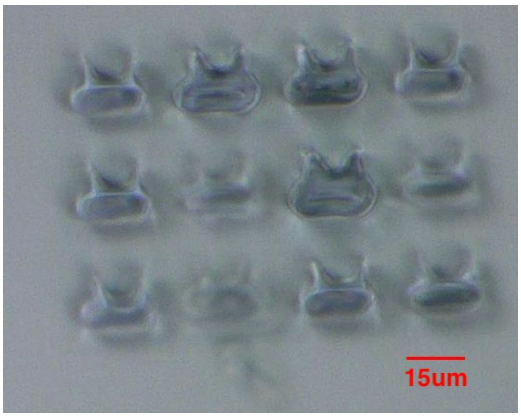

Figure 4.32: IP-PDMS dose test on Silicon chip

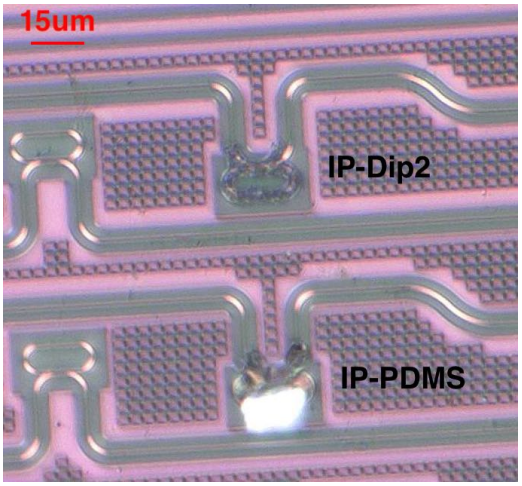

Figure 4.33: IP-Dip2 and IP-PDMS coated MRR

Finally, by using a power of 65% and making 4 repetitions, a 3μm height and 2μm width IP-PDMS patterned was printed on an add drop MRR that will be used for measurement as shown in figure 4.34. This time, the edge bumps did not occur because the power was quite low to not cause excess heat while repeating many times the printing and gradually cure the IP-PDMS. Later on, after the 5min development in IPA, additional IPA and PGMEA drops were used to remove remaining uncured resin with an air gun. For a full IP-PDMS coating of the MRR, the same amount of power of 65% was used but with 6 repetitions instead. This is because the location of the focal point always changes with chip inclination and positioning, so the amount of repetitions may differ.

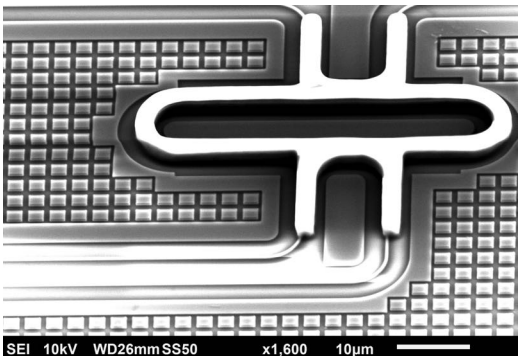

Figure 4.34: SEM image of patterned IP-PDMS

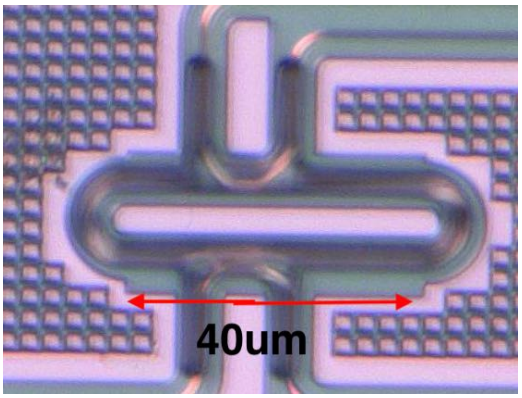

Figure 4.35: Microscope image of patterned IP-PDMS

4.3. Ultrasound measurements

Below, are displayed the ultrasound measurement with different waveguide cladding configurations: No cladding, fully coated and patterned S1805, fully coated and patterned IP-PDMS, thus 5 ultrasound measurements in total. At the end of this section, the computed sensitivities, which are the pressure induced resonance shifts will be put in table 4.2 for comparison. Plots of the AC signals with removed constant DC are plotted with error bars to show the deviation in peak values from noise rms. For all measurements, a laser power of 12dbm with an attenuator of 10db was used. Plots of the filtered frequency sweeps and their gradients were given to visualize the average DC coupling levels and values of the flank wavelength slopes. A lower DC coupling level would mean a lower flank wavelength slope and a lower observable slope of the measured peaks. DC coupling levels frequently change from experiments to experiments but they do not pose a problem for comparing sensitivities because the effect of DC coupling is cancelled as explained by equation 3.3, in section 3.2.

No cladding

With no cladding, the upper part of the Si core waveguide is water and the lower part is SiO_2. The maximum resonance wavelength slope at the flank wavelength is -11.0 [V/nm]. The slope from the quadratic fit is 7.4e-05 [V/kPa] and the computed resonance shift from it is -6.7e-06 [nm/kPa]. The slope from the linear fit from the origin point (0,0) is 8.7e-05 [V/kPa] and the computed resonance shift from it is -8.0e-06 [nm/kPa]. Based on a computed noise RMS of 0.0044 [V], the computed limit of detection (LOD) from the quadratic fit is 59.9[kPa] and the computed LOD from the linear fit from the origin point (0,0) is 50.606[kPa]

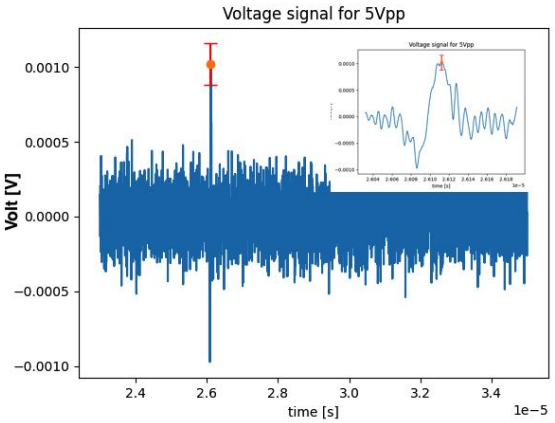

Figure 4.36: AC time signal

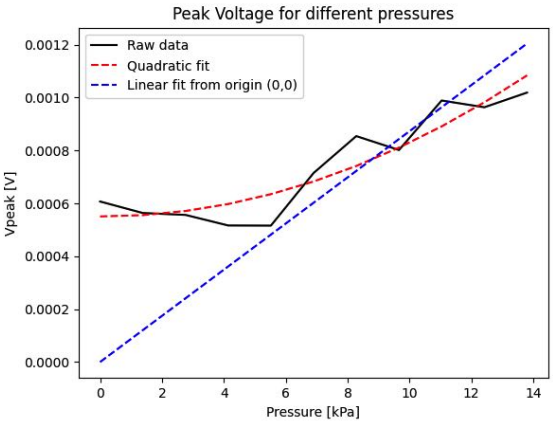

Figure 4.37: Measured peaks and fits

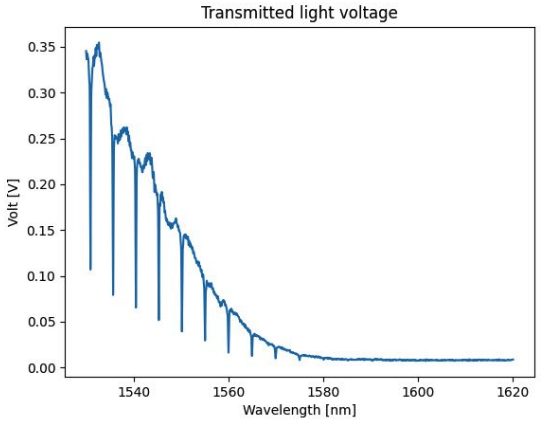

Figure 4.38: Frequency sweep

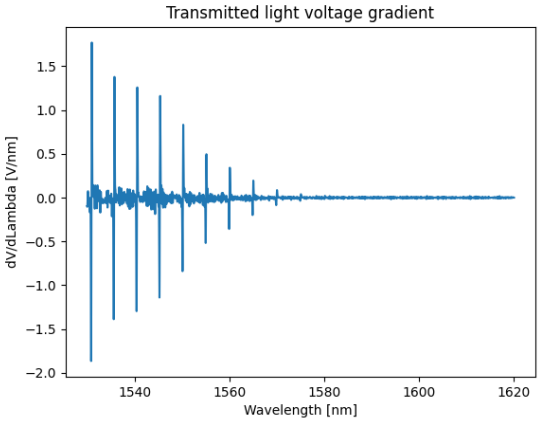

Figure 4.39: Gradient of frequency sweep

S1805 full coat

The maximum resonance wavelength slope at the flank wavelength is -16.3 [V/nm]. The slope from the quadratic fit is 0.00012 [V/kPa] and the computed resonance shift from it is -7.4e-06 [nm/kPa]. The slope from the linear fit from the origin point (0,0) is 9.6e-05 [V/kPa] and the computed resonance shift from it is -5.9e-06 [nm/kPa]. Based on a computed noise RMS of 0.0044 [V], the computed LOD from the quadratic fit is 36.6[kPa] and the computed LOD from the linear fit from the origin point (0,0) is 46.2[kPa]. The wave shape is a slightly better than the configuration without cladding.

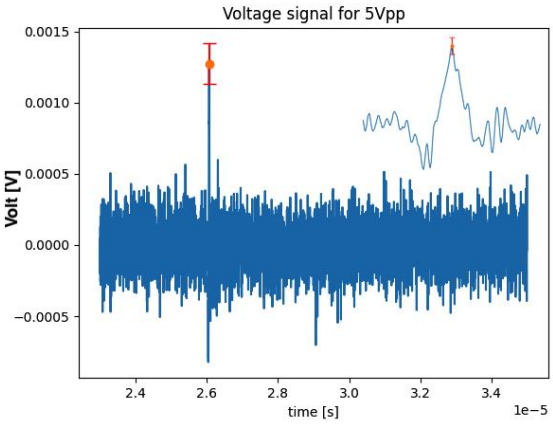

Figure 4.40: AC time signal

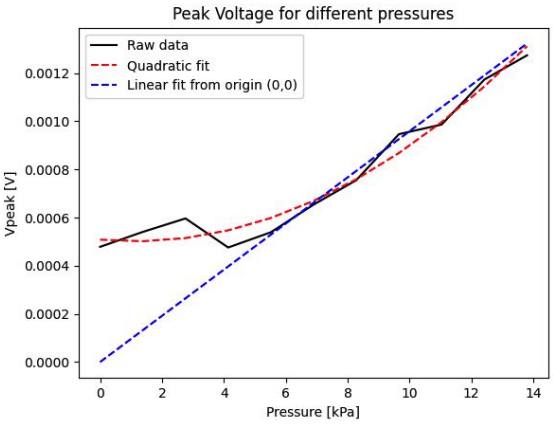

Figure 4.41: Measured peaks and fits

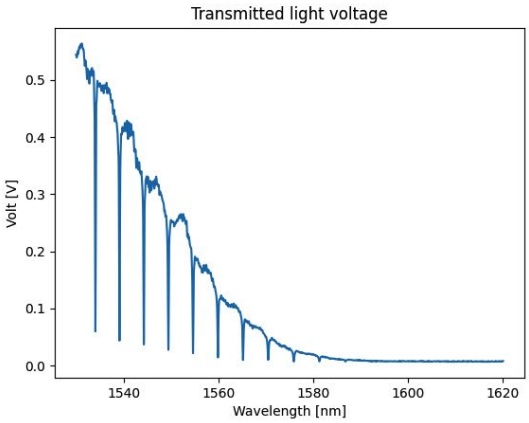

Figure 4.42: Frequency sweep

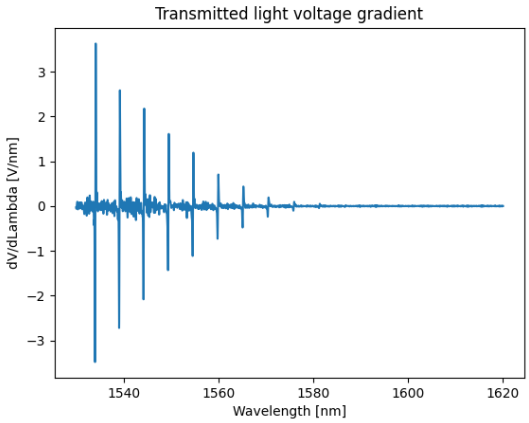

Figure 4.43: Gradient of frequency sweep

S1805 patterned cladding

The maximum resonance wavelength slope at the flank wavelength is -9.253 [V/nm]. The slope from the quadratic fit is 8.23e-05 [V/kPa] and the computed resonance shift from it is -8.9e-06 [nm/kPa]. The slope from the linear fit from the origin point (0,0) is 0.00010109 [V/kPa] and the computed resonance shift from it is -10.9e-06 [nm/kPa]. Based on a computed noise RMS of 0.0043 [V], the computed LOD from the quadratic fit is 52.1[kPa] and the computed LOD from the linear fit from the origin point (0,0) is 42.5[kPa]. The wave shape is similar to the fully coated S1805, but the overall shape is defined more clearly.

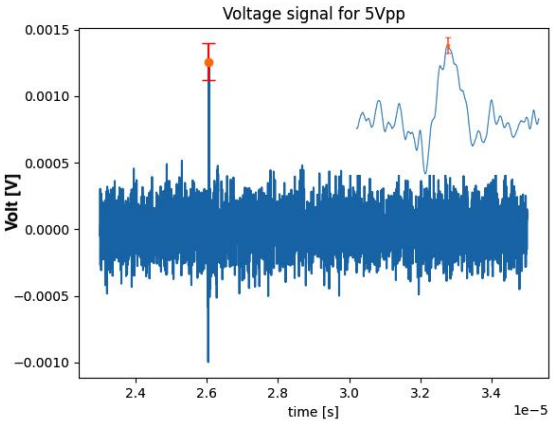

Figure 4.44: AC time signal

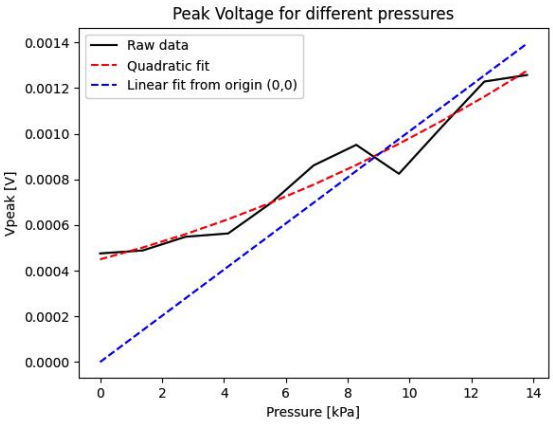

Figure 4.45: Measured peaks and fits

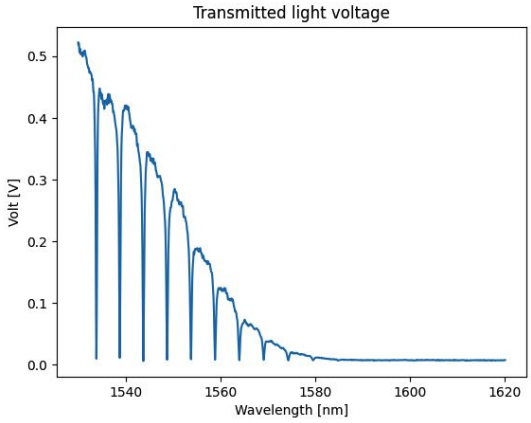

Figure 4.46: Frequency sweep

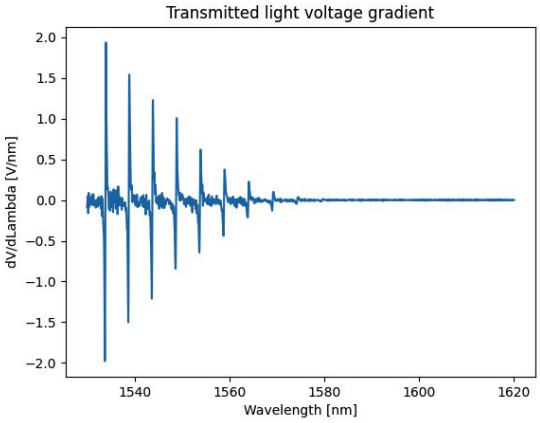

Figure 4.47: Gradient of frequency sweep

IP-PDMS full coat cladding

The maximum resonance wavelength slope at the flank wavelength is -12.1 [V/nm]. The slope from the quadratic fit is 0.00015 [V/kPa] and the computed resonance shift from it is -12.6e-06 [nm/kPa]. The slope from the linear fit from the origin point (0,0) is 0.00019 [V/kPa] and the computed resonance shift from it is -15.5e-06 [nm/kPa]. Based on a computed noise RMS of 0.0044 [V], the computed LOD from the quadratic fit is 29.4[kPa] and the computed LOD from the linear fit from the origin point (0,0) is 23.9[kPa]. The wave shape is quite smooth. However, the shape of it is different than the other measurements because the maximum peak absolute value of 1.2mV is meant to be much large than the peak at -1mV (see figure 4.48. This may be caused by the positioning of the US transducer with respect to the chip.

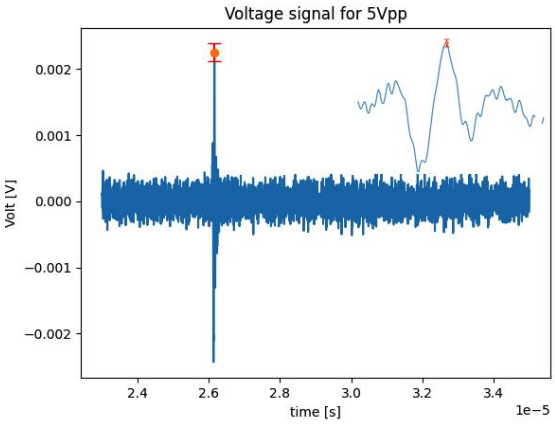

Figure 4.48: AC time signal

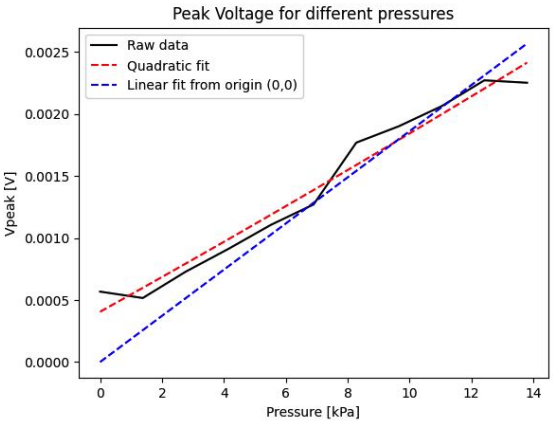

Figure 4.49: Measured peaks and fits

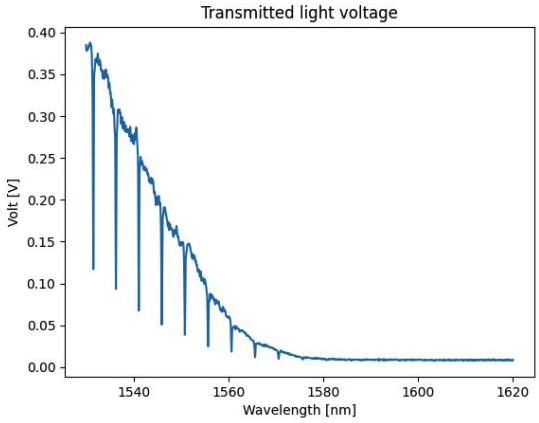

Figure 4.50: Frequency sweep

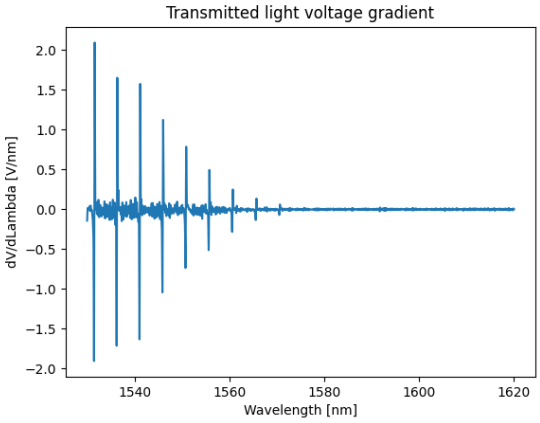

Figure 4.51: Gradient of frequency sweep

IP-PDMS patterned cladding

The maximum resonance wavelength slope at the flank wavelength is -15.5 [V/nm]. The slope from the quadratic fit is 0.00051 [V/kPa] and the computed resonance shift from it is -33.1e-06 [nm/kPa]. The slope from the linear fit from the origin point (0,0) is 0.00048 [V/kPa] and the computed resonance shift from it is -31.1e-06 [nm/kPa]. Based on a computed noise RMS of 0.0045 [V], the computed LOD from the quadratic fit is 8.7[kPa] and the computed LOD from the linear fit from the origin point (0,0) is 9.3[kPa]. The peak shape is very smooth due to the high amplitude of the signal so the noise fluctuations are less observable.

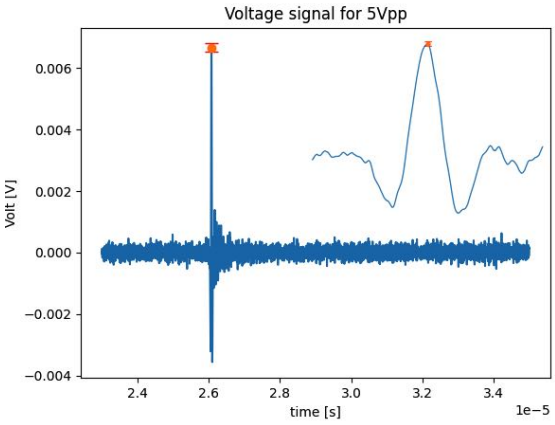

Figure 4.52: AC time signal

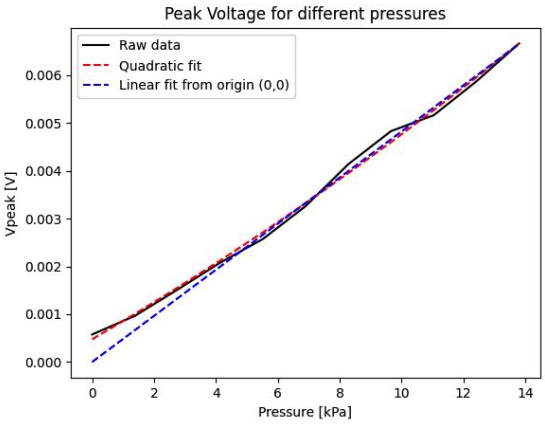

Figure 4.53: Measured peaks and fits

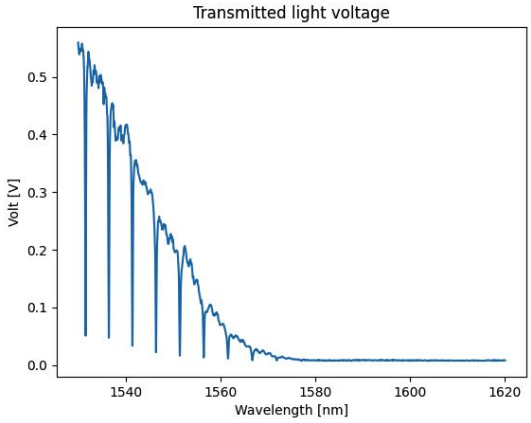

Figure 4.54: Frequency sweep

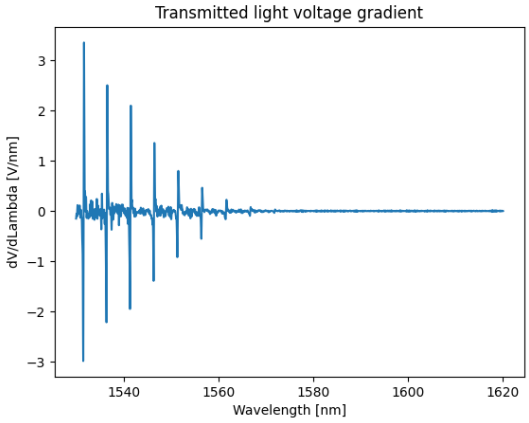

Figure 4.55: Gradient of frequency sweep

Below is attached a summary of the ultrasound measurements that displays the resonance shifts for both fits.

Cladding	Shift (Quadratic fit) [fm/kPa]	Shift (Fit at origin) [fm/kPa]	Simulation [fm/kPa]
No cladding	-6.7	-8.0	-2.6
Full S1805	-7.4	-5.9	-2.8
Patterned S1805	-8.9	-10.9	-8.7
Full IP-PDMS	-12.6	-15.5	-6.7
Patterned IP-PDMS	-33.1	-31.1	-14.4

Table 4.2: Summary of ultrasound measurements

5

Discussion

5.1. Fabrication methods

After several dose tests with the laser cutter, the limits of what the device could achieve were reached. The finest and cleanest cut achieved had a width of 14.8μm with a brown edge of 5.2μm as shown in figure 4.10. The brown edge width remained too large compared to the 0.45μm width of the core waveguide. Based on the camera view, even if a PDMS coated waveguide was to be laser etched by etching both sides one by one and using an offset to cut at a distance from the waveguide and let only the brown edge region reach the waveguide, the alignment would be quite difficult and risks of reaching the Si02 substrate are still high because of the laser power. The final attempt of using more defocus and adding repetitions, has made the cutting process unstable and caused irregular line cuts. Therefore, there were no further possibilities with this fabrication method and was dismissed.

Moving to the laser writer, the dose tests made by Paulina (figure 4.18, 4.14) have shown that using the minimum feature size of 1μm for both resists made accurate prints. Nonetheless, alignment remained an issue despite the fact that it was indicated in the data sheet that the alignment positioning accuracy was 500nm, thus with a 2μm width pattern, the ring core should still have been fully covered with the pattern despite misalignment. Since it was not possible to investigate potential reasons for that on the machine, the print was deemed satisfactory for ultrasound measurements. In terms of easy of use, scalability for manufacturing, and size of printable region, this would be a preferred method.

The last fabrication method using the Nanoscribe was deemed to be the most successful despite the many challenges that came along working with IP-PDMS. It was suggested by experienced users that IP-PMDS is not made to be used with the x63 objective and quite difficult to work with. Thus, several doses tests were done with IP-PDMS in comparison to IP-DIP2 to gain experience and make a new printing procedure method that tackles challenges of alignment, feature size, edge bumps, vision of features, etc. Patterns were printed with a good width accuracy because the width measured with the microscope was 2μm as designed in the model. More tests could be done to improve the fabrication recipe and attempt to print features even smaller than the 2μm. There are still some drawbacks with this method such as having only a small printing area which prevents from printing many rings at the same time. The alignment procedure takes time and requires several steps before printing. Furthermore, IP-PDMS is quite transparent, and when using heights of around 2μm, the prints cannot be seen on the camera, either higher heights, multiple print repetitions or increasing laser power must be done to observe something. However, increasing the power will cause edge bumps from the generated heat. If printing on a chip, uneven surfaces or height tilts will require changing number of repetitions or even power so recipes will always need adjustments. In the future, if working with IP-PDMS, the user should bear in mind that the refractive index of IP-PDMS is very similar to glass which leads to problem such as the nanoscribe finding wrong or no interfaces at all. Either another substrate should be used or a non transparent glass can be used but the interface will have to be found manually. Finally, uncured IP-PDMS can still remain sticking to printed structures despite development so additional washing with IPA/PGMEA is needed. Overall, sufficient experience is required before getting good prints.

Method	Polymers	Minimum feature achieved [um]
Laser cutter	PDMS	14.8
Laser writer	S18013/S1805	1
Nanoscribe	IP-Dip/IP-Dip2/IP-PDMS (x63 obj)	less than 1

Table 5.1: Summary of fabrication methods

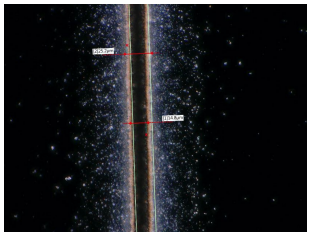

Figure 5.1: Best laser cut

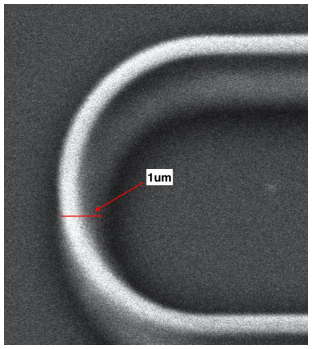

Figure 5.2: Best laser writer pattern print

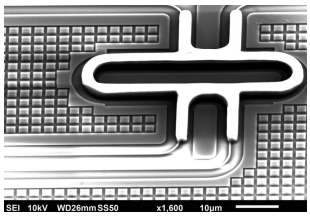

Figure 5.3: Best nanoscribe pattern print

5.2. Ultrasound measurements and COMSOL simulation comparison

There is a remarkable difference of sensitivities between a patterned and non-patterned cladding in both COMSOL and US measurements. The main source of sensitivity can be attributed to photo-elasticity because the used cladding dimensions were large enough to have negligible deformation effects. This can be seen on figure 2.16, which was used to compare the photo-elastic and deformation effects with different cladding heights and widths. Looking at the COMSOL plots of the relative change of refractive index (n_x-n_y) of patterned S1805 and IP-PDMS (fig 4.3 and 4.5), the main difference between them is that photo-elasticity mainly occurs inside the core with S1805 and outside the core with IP-PDMS. For both materials, location of photo-elastic occurs near regions with high electric field intensities which are either at the middle of the core or at the left and right edges of the core (see figure 4.1). The use of a patterned cladding, allowed more photo-elasticity to occur at that region which is known to be more sensitive to changes, as previously explained in chapter 1 in reference [12]. The difference between the patterned and non-patterned IP-PDMS is more visible than with S1805 because of its higher stress optic coefficients. It would be suggested to use smaller cladding widths to increase sensitivity even further by causing the photo-elasticity to be nearer to the core lateral edges.

Overall, tables 4.1 and 4.2 have shown that the ultrasound has reduced the n_{eff}, inducing a negative resonance shift (hence the minus sign) for all claddings. They have demonstrated that patterning has considerably increased sensitivity by approximately a factor of 2 between a non-patterned and a patterned cladding for both S1805 and IP-PDMS. The sensitivity values between the COMSOL and ultrasound measurements are of similar orders of magnitudes but with some numerical differences. This was something expected because, as explained in chapter 2, most mechanical properties where unknown as well as the stress-optic coefficients of S1805 and IP-PDMS. Based on the assumed photo-elastic coefficients, the COMSOL model can give wrong sensitivity results because the main source of it comes from photo-elasticity. These numerical differences can happen in 2 ways. First, it could be that the photo-elastic coefficients are reducing the effect of deformation such that if the deformation causes a negative change of n_{eff} while the photo-elasticity causes a positive change, the absolute value of the total change is lower than without the photo-elastic effect. The second way, could be that the photo-elastic coefficients are very small so only deformation effects cause a change or refractive index. The assumed coefficients cannot be sufficiently realistic by only trying to approximate the values for S1805 and IP-PDMS around known values of the lowest and maximum stress optic coefficient values (found in literature). Yet, there are other factors that could also explain such differences. The first factor could

be the change of water refractive index from pressure. Even if assumed to be negligible because of the low US pressure, it may still have an noticeable effect on the computed electric field and n_{eff} as well. Concerning the US measurements, difference of sensitivities with COMSOL could come from the noise effect on the fitted lines. When noise dominates the US signal, fluctuations of data points occur and will influence the slope value at the linear region for high V_{pp}. Overall, it is fair to say that the COMSOL model is good for a qualitative analysis, as the sensitivity improvement trends are similar to the trends observed with the ultrasounds measurements table 4.2.

Concerning the numerical values of the sensitivity, the best one is from the patterned IP-PDMS with a value of -33.1 [fm/kPa]. This is near the sensitivity of a sensor designed by Zarkos et al [25] with 40 [fm/kPa]. However, it remains much lower than the one designed by W.Westerveld et al [12] with a sensitivity of 38[fm/Pa]. The main reasons for such a high sensitivity is its unique design with a suspended membrane. It gives little mechanical resistance for motion and will allow more deflection. Also, the electric fields are concentrated near the gap between the core and membrane which makes it very sensitive as the membrane moves. It is not very useful at this stage to try to compare sensitivities values with these papers, because in addition to their different design features, if considering just the plain rings, they can have different intrinsic sensitivities (depending on design and material). As seen in table 4.2, the intrinsic sensitivity of the ring without cladding is quite low, which explains why, not very high numbers are achieved. Then, it is more relevant to compare sensitivities only between the different cladding configurations. This also concerns the LOD values that were given to show what would be minimum detectable pressures based on the computed sensitivities from the fits. They demonstrate that as sensitivity increases, the minimum detectable pressure would decrease.

Concerning AC peak shapes, it was noticed that for the full coat IP-PDMS with the 6μm height, the peak shape of the AC signal was different from other measurements. The positioning of the US transducer with respect to chip, might have been with a small angle orientation instead of being orthogonal, which could have caused the peak shape difference. Unfortunately, it is not clear what happened at the chip surface, to understand what causes the peak change. But this observed phenomenon raises questions about the hydro-static pressure assumption at the chip where in this case even if the pressure wave arrives at a small angle, there should not be any noticeable differences in the way the cladding would deform.

Looking at the fitted lines from the ultrasound measurements, for all measurements there is approximately a difference of 2.1 [fm/kPa] of resonance shifts between the quadratic fit and linear fit from the origin. For the least sensitive devices, that difference of fit sensitivity is considerable with respect to the average sensitivity value between the 2 fits. At low input V_{pp}, the peak voltage level V_{peak} is expected to be 0V but instead it is at 4mV. This is caused by the noise which has a rms level of 4.4mV and causes significant difference when comparing the slopes of the 2 fits (see fig 4.37). If sensitivity is high (such as patterned IP-PDMS), amplitude values are higher and less data points will be in the noise regime. A linear fit such $y = ax$ should provide a very similar slope to the quadratic fit in the linear regime. However it cannot be used with low sensitivity cladding configurations (no cladding) because there are more data points within the noise regime and will corrupt the fit slope value. Thus the quadratic fit is more suitable to fit both the noise and linear regimes and resembles very much figure 3.19. It could be suggested to use a filtering of the data points to obtain smoother curves. The deviations between raw and filtered data can be observed to assess the quality of the filter. Another suggestion, is to use more averaging during signal acquisition, which would be the most effective method for getting more precise peak measurements.

Finally, since the main source of sensitivity comes from photo-elasticity, the location of internal stresses will depend on the cladding geometry. The use of a COMSOL simulation can be a very effective tool for experimenting with different geometries to cause more photo-elasticity near a high electric field region. Despite the differences in sensitivity values between COMSOL and US measurements, the improvement trends are similar. Therefore, the simulation model could be used to start experimenting with new cladding shapes and with the 3D printing capabilities of the nanoscribe, the newly designed shapes could be made for experimental measurements. Currently, one challenge of photo-acoustic imaging is the limited imaging depth. Higher sensitivities are required to be able to detect weaker US signals that come from lower tissue depths. When designing sensors, the simplicity of applying polymer on top of a micro ring, can be an effective alternative to relying on complex designs to increase sensitivity.

The best achievable sensitivity using a polymer cladding has yet to be determined and the foundations for fabricating a polymer pattern and analysing cladding geometries with COMSOL were established.

6

Conclusion and outlook

This thesis project consisted of studying the effect of a patterned polymer cladding on MRRs to find out if it would improve their sensitivity to ultrasounds.

First, a COMSOL simulation was done with parametric sweeps of cladding height and width to understand at which dimensions, photo-elastic or deformation effects would be the dominant cause of US sensitivity. Simulations with different cladding configurations (based on fabricated geometries) were done to derive the induced resonance shifts from pressure. The sensitivity results of the simulations showed almost a doubling of sensitivity between non-patterned and patterned claddings (S1805 and IP-PDMS). To fabricate a polymer pattern on top of a MRR, 3 fabrication methods were attempted and a successful print was made with the nanoscribe. Much efforts were put to overcome challenges when using IP-PDMS with the x63 objective such as edge bumps, alignment, interface finding, lack of camera vision etc. Though this device is more difficult to work with, it has a remarkable advantage over the laser cutter and laser writer as it is the only device that produces very small 3D printed structures. If more complex cladding geometries were found to increase US sensitivity, they could then be produced with the nanoscribe. The developed fabrication recipe for using IP-PDMS with the x63 objective can be useful for other research projects if small 3D structures need to be produced from a soft polymer. Looking at the US measurements done for the different cladding configurations, it was also demonstrated that US sensitivity has almost doubled between a non-patterned and patterned cladding. There are numerical differences of sensitivity between the simulation and US measurement results. This is due to the limitations of the COMSOL model where many mechanical properties and stress optic coefficients were unknown so assumptions had to be made. Nonetheless, the sensitivity values of both measurements have similar improvement trends and orders of magnitudes. Therefore, it would be recommended to use the COMSOL model to experiment with new cladding geometries to direct more refractive index change (from photo-elasticity) towards high electric field regions. Achieving higher sensitivities would allow to detect weaker US signals during photo-acoustic imaging and image at lower depths in tissues. By applying a polymer cladding on top of a MRR, it could be a simple and effective method for increasing sensitivity and the analysis and fabrication methods were demonstrated in this thesis to achieve this goal.

Bibliography

[1] Yoav Hazan et al. “Silicon-photonics acoustic detector for optoacoustic micro-tomography”. In: *Nature Communications* 13.1 (Dec. 2022). ISSN: 20411723. DOI: 10.1038/s41467-022-29179-7.

[2] Tamar Harary, Yoav Hazan, and Amir Rosenthal. “All-optical optoacoustic micro-tomography in reflection mode”. In: *Biomedical Engineering Letters* 13.3 (Aug. 2023), pp. 475–483. ISSN: 2093985X. DOI: 10.1007/s13534-023-00278-8.

[3] Shankar Kumar Selvaraja and Purnima Sethi. “Review on Optical Waveguides”. In: *Emerging Waveguide Technology*. InTech, Aug. 2018. DOI: 10.5772/intechopen.77150.

[4] Graham Reed and A Knights. *Silicon Photonics: An Introduction*. 2004.

[5] *6.007 Electromagnetic Energy: From Motors to Lasers (MIT Lecture)*. 2011.

[6] Georg Wissmeyer et al. *Looking at sound: optoacoustics with all-optical ultrasound detection*. Dec. 2018. DOI: 10.1038/s41377-018-0036-7.

[7] W. Bogaerts et al. “Silicon microring resonators”. In: *Laser and Photonics Reviews* 6.1 (Jan. 2012), pp. 47–73. ISSN: 18638880. DOI: 10.1002/lpor.201100017.

[8] Giuseppe A Cirino et al. “Simulation and fabrication of silicon nitride microring resonator by DUV lithography Simulation and fabrication of silicon nitride microring resonator by DUV lithography Simulation and Fabrication of Silicon Nitride Microring Resonator by DUV Lithography”. In: (2016), pp. 1–4. DOI: 10.1109/SBMicro.2016.7731346{\"{i}}. URL: https://hal.science/hal-01398394.

[9] David J Lockwood and Lorenzo Pavesi. *Silicon Photonics II: Components and Integration (Topics in Applied Physics)*.

[10] Winnie N. Ye et al. “Birefringence control using stress engineering in silicon-on-insulator (SOI) waveguides”. In: *Journal of Lightwave Technology* 23.3 (Mar. 2005), pp. 1308–1318. ISSN: 07338724. DOI: 10.1109/JLT.2005.843518.

[11] R Tufan Erdogan et al. “Enhancing the sensitivity of silicon photonic ultrasound sensors by optimizing the stiffness of polymer cladding”. In: (2023).

[12] Wouter J. Westerveld et al. “Sensitive, small, broadband and scalable optomechanical ultrasound sensor in silicon photonics”. In: *Nature Photonics* 15.5 (May 2021), pp. 341–345. ISSN: 17494893. DOI: 10.1038/s41566-021-00776-0.

[13] S. M. Leinders et al. “A sensitive optical micro-machined ultrasound sensor (OMUS) based on a silicon photonic ring resonator on an acoustical membrane”. In: *Scientific Reports* 5 (Sept. 2015). ISSN: 20452322. DOI: 10.1038/srep14328.

[14] Bo Fu et al. *Optical ultrasound sensors for photoacoustic imaging: a narrative review*. Feb. 2022. DOI: 10.21037/qims-21-605.

[15] Qiangzhou Rong et al. “High-Frequency 3D Photoacoustic Computed Tomography Using an Optical Microring Resonator”. In: *BME Frontiers* 2022 (Jan. 2022). ISSN: 27658031. DOI: 10.34133/2022/9891510.

[16] Zuoqin Ding et al. “Broadband Ultrasound Detection Using Silicon Micro-Ring Resonators”. In: *Journal of Lightwave Technology* 41.6 (Mar. 2023), pp. 1906–1910. ISSN: 15582213. DOI: 10.1109/JLT.2022.3227064.

[17] Michael Nagli et al. “Silicon-photonics focused ultrasound detector for minimally invasive optoacoustic imaging”. In: *Biomedical Optics Express* 13.12 (Dec. 2022), p. 6229. ISSN: 2156-7085. DOI: 10.1364/boe.470295.

[18] Shipley. *MICROPOSIT S1800 SERIES PHOTORESISTS 2 INSTRUCTIONS FOR USE*. Tech. rep. 2016.

[19] Sergei M Aizikovich et al. *Advanced Structured Materials Modeling, Synthesis and Fracture of Advanced Materials for Industrial and Medical Applications*. Tech. rep. URL: http://www.springer.com/series/8611.

[20] Resmi Ravi Kumar et al. "Enhanced Sensitivity of Silicon-Photonics-Based Ultrasound Detection via BCB Coating". In: *IEEE Photonics Journal* 11.3 (June 2019). ISSN: 19430655. DOI: 10.1109/JPHOT.2019.2908013.

[21] Nanoguide. *IP-PDMS – NanoGuide*. 2024.

[22] Sedat Dogru et al. "Poisson's ratio of PDMS thin films". In: *Polymer Testing* 69 (Aug. 2018), pp. 375–384. ISSN: 01429418. DOI: 10.1016/j.polymertesting.2018.05.044.

[23] Heidelberg Instruments. *MLA 150 THE ADVANCED MASKLESS ALIGNER*. Tech. rep.

[24] Nanoguide. *Photonic Professional GT2*. 2024.

[25] Panagiotis Zarkos et al. "Fully Integrated Electronic-Photonic Ultrasound Receiver Array for Endoscopic Applications in a Zero-Change 45-nm CMOS-SOI Process". In: *IEEE Journal of Solid-State Circuits* 58.6 (June 2023), pp. 1719–1734. ISSN: 1558173X. DOI: 10.1109/JSSC.2022.3222829.

A

GDS Mask and 3D SLT file generator Py Code

```
import gdsfactory as gf
from gdsfactory.generic_tech import get_generic_pdk
import shapely as sp
import subprocess
from shapely.geometry import LineString, Polygon, MultiPolygon
gf.config.rich_output()
gf.CONF.display_type = 'klayout'
PDK = get_generic_pdk()
PDK.activate()

# Import gds file
imp = gf.import_gds(gdspath="ab77core.gds") # waveguide with added box region
imp2 = gf.import_gds(gdspath="abwaveguideonly.gds",) # waveguide
markerimp=gf.import_gds(gdspath="boxedup2.gds") # markers for small rr3
flatedit=gf.import_gds(gdspath="flatedit.gds") # whole chip

# offset of 0.175 for 0.8 width then 0.375 for 1.2 then 0.525 for 1.5 then 0.775 for 2
a= [0.175, 0.425, 0.575, 0.775, 0.975, 0.275] # will be used for offset values
b= [0.8, 1.3, 1.6, 2, 2.4, 1] # will be used to make file name

# Create component for extracting negative with a border
c=gf.Component("Initial")
c1=c << imp
border=5 # Choose border size
invert=gf.geometry.invert(c,border=(border),layer=(3, 0),)
# Put the boolean in a new component to remove side rectangle edges
inverted=gf.Component('Inverted')
c2=inverted << invert
#c3=inverted.add_ref(component=invert,name)
# remove the side polygons by adding 2 rectangles and doing boolean
rect1=gf.components.rectangle(size=[(border+4),(inverted.xmax-inverted.xmin)],layer=(2,0),
    centered=False) # change to y max in case
# Make a component of 2 rectangles to be removed from 'Inverted' component
rectangles=gf.Component('Rectangles')
r1=rectangles<<rect1
r1.move(origin=(0,0),destination=((inverted.xmin-10),(inverted.ymin-2)))
r2=rectangles << rect1
r2.move(origin=(0,0), destination=((inverted.xmax-border+10),inverted.ymin))
boolean=gf.geometry.boolean(A=inverted,B=rectangles,operation='A-B')
# Final model to be put in a new component
finished=gf.Component('Final')
c3=finished << boolean
c3.mirror(p1=[1,1],p2=[1,2]) # mirror along y axis

# Use 'for' for make offsets of different sizes and generate the gds files
invertion=input("Would␣you␣like␣to␣invert␣the␣geometry␣(y/n)␣?␣")
```

```
stl=input("Would␣you␣like␣to␣make␣an␣stl␣file␣as␣well␣(y/n)␣?␣")

for x in range(0, 6):
    # Extract offset geometry
    if invertion=='y':
        Texvert = gf.geometry.offset(finished, distance=(-a[x]), precision=1e-6, layer=(9, 0)
            )
    else:
        Texvert = gf.geometry.offset(finished, distance=(-a[x]), precision=1e-6, layer=(9, 0)
            )
        Texvert=gf.geometry.invert(Texvert,border=-0.1) # to re-invert the component to get
            coating on the wavequide
    # Make component to include offset geometry and flatten everything
    # @gf.cell
    # def claddingandmarkers():
    off=gf.Component('offsetted')
    inv = off << Texvert
    # mark= off << markerimp
    # guide= off << imp2
    # Include other layers for checking the
    # c2 = off << imp2 # include the original waveguide
    # c3 = off << markerimp # include the markers
    # c4 = off << flatedit
    off=off.flatten()
        # return off
    # off=claddingandmarkers()
    wi=f"ab77mir_{b[x]}.gds" # make name of file
    off.write_gds(wi) # create gds file of modified model, use gdsiistl.py from github and
        make the right cell name is written in the code so that the extrusion works
    if stl=='y':
        # subprocess.Popen(f'python3.10 gdsiistl.py {wi}')
        print('making␣stl')
        command = ['python3.10', 'gdsiistl.py', f'{wi}'] # the argument is the space and then
             something you write to you can use f'{wi}'
        process = subprocess.Popen(command)

off.show() # show the model on klayout
```